SANDIA REPORT
SAND2013-7833
Unlimited Release
September 2013

Aerosol Characterization Study Using Multi-Spectrum Remote Sensing Measurement Techniques

Crystal C. Glen, Randal L. Schmitt, Alice Sobzcak, Andres Sanchez, Matt Tezak, Mark Johnson, Gabriel Lucero, Brandon Servantes

Sandia National Laboratories

Aerosol Characterization Study Using Multi-Spectrum Remote Sensing Measurement Techniques

Crystal C. Glen, , Andres Sanchez, Gabriel Lucero,
WMD Contraband Detection

Randal L. Schmitt, Alice Sobzcak, Mark Johnson
Laser, Optics, and Remote Sensing

Matt Tezak
Chemical and Biological Systems

Brandon Servantes
Fire and Aerosol Sciences

Sandia National Laboratories
P.O. Box 5800
Albuquerque, New Mexico 87185-MS1148

Abstract

A unique aerosol flow chamber coupled with a bistatic LIDAR system was implemented to measure the optical scattering cross sections and depolarization ratio of common atmospheric particulates. Each of seven particle types (ammonium sulfate, ammonium nitrate, sodium chloride, potassium chloride, black carbon and Arizona road dust) was aged by three anthropogenically relevant mechanisms: 1. sulfuric acid deposition, 2. toluene ozonolysis reactions, and 3. m-xylene ozonolysis reactions. The results of pure particle scattering properties were compared with their aged equivalents. Results show that as most particles age under industrial plume conditions, their scattering cross sections are similar to pure black carbon, which has significant impacts to our understanding of aerosol impacts on climate. In addition, evidence emerges that suggest chloride-containing aerosols are chemically altered during the organic aging process. Here we present the direct measured scattering cross section and depolarization ratios for pure and aged atmospheric particulates.

CONTENTS

FIGURES

NOMENCLATURE

NH_4NO_3	Ammonium Nitrate
$(NH_4)_2SO_4$	Ammonium Sulfate
APD	Accurate Peak Detector
APS	Aerodynamic Particle Sizer
ARD	Arizona Road Dust
BC	Black Carbon
cfm	Cubic Feet per Minute
FBAG	Fluidized Bed Aerosol Generator
HEPA	High-Efficiency Particulate Air
ICCD	Intensified Charge-Coupled Device
LIDAR	Light Detection and Ranging
LIF	Laser Induced Fluorescence
lpm	Liters per Minute
mJ	mili-Joule
Nd:Yag	Neodymium Yttrium Aluminum Garnet
N_2	Nitrogen
O_3	ozone
PSD	Particle Size Distribution
KCL	Potassium Chloride
NaCl	Sodium Chloride
sr	Steradian

1. EXECUTIVE SUMMARY

Primary emissions of atmospheric aerosol from both natural and anthropogenic sources comprise the portion of the ambient suspended particle size distribution known as the coarse mode particles, those particles that are sized greater than roughly 0.7 μm. These aerosols, due to their large sizes, are of major importance in atmospheric scattering of incident light. Mineral dusts have been known to transport long distances across the pacific from Asia (Duce, Unni et al. 1980, Uematsu, Duce et al. 1983). In addition, convective mechanisms in the atmosphere can loft burning biomass and other anthropogenic plumes into the upper atmosphere facilitating transport of these large aerosol sizes (Andreae, Artaxo et al. 2001, Colarco, Schoeberl et al. 2004). It is therefore important to understand how atmospheric aging of these primary particles alters their optical scattering properties to improve model predictions, aid in understanding satellite retrievals of particulates, and advance our understanding of LIDAR-measured plume age.

We have a developed a unique, state-of-the-art laboratory-based instrument to measure and study the optical backscatter properties of aerosol under well controlled and well characterized conditions. The instrument consists of a short-standoff bi-static LIDAR system coupled to a sealed, flowing aerosol chamber that provides optical access to the aerosol. The LIDAR system measures the elastic backscatter cross section and depolarization ratio of disseminated aerosol at 355 nm and 1064 nm. Seven atmospherically relevant primary aerosols (ammonium sulfate, ammonium nitrate, laboratory-grade black carbon, potassium chloride, sodium chloride, and Arizona road dust) were generated and aged according to three mechanisms: 1. sulfuric acid deposition, 2. toluene ozonolysis reactions, and 3. m-xylene ozonolysis reactions. Each aerosol type was aged for approximately 20 minutes in elevated gaseous concentrations to mimic the long-term conversion of primary aerosol to secondary aerosol, aerosol formed by both adsorption and absorption of low-volatility gases in the atmosphere (Odum, Hoffmann et al. 1996, Bahreini, Keywood et al. 2005, Hallquist, Wenger et al. 2009). Both toluene and m-xylene oxidation by ozone lead to products known to produce high yields of secondary organic aerosol (SOA) (Kroll, Ng et al. 2005, Donahue, Robinson et al. 2009), and seed aerosol have been shown to enhance the nucleating behavior of organics in the atmosphere (Czoschke, Jang et al. 2003). Sulfuric acid is commonly formed by the oxidation of sulfur dioxide in the presence of water and is also known to exist in the particle phase within anthropogenic plumes (Rodhe, Crutzen et al. 1981).

This study shows that aged aerosol have a tendency to scatter 355-nm and 1064-nm light less efficiently than their pure forms. In many of the cases studied, a greater than 75% reduction in optical scattering cross section was observed from organic aging mechanisms, consistent with previous studies investigating the optical properties of condensed carbonyl and glyoxal, a toluene and m-xylene oxidation product (Kroll, Ng et al. 2005, Shapiro, Szprengiel et al. 2009). In most cases, the measured cross section for organically aged aerosol is near that for pure black carbon aerosol. Sulfuric acid deposition on the particle surface also showed a tendency to produce lower values for optical scattering cross section with the exception of sulfuric acid interactions with black

carbon. Ammonium sulfate aerosol exhibited the least response to all aging mechanisms. Results also indicate that chloride-based aerosol react internally with organic vapors leading to potential chemical composition changes that result in a more absorptive aerosol particle. In this report, we describe the optical measurement system and aerosol chamber, including the aerosol aging apparatus, and we present the results of measured 355-nm and 1064-nm optical scattering cross section and depolarization ratio for fresh and aged primary aerosol.

2. EXPERIMENTAL SETUP

2.1. Aerosol Flow System and Aging Chamber

The aerosol flow chamber described in this chapter (illustrated in Figure 1) is specially designed to provide optical access to a uniformly mixed aerosol with stable particle size distribution (PSD) both along the axis of the chamber and radially. The flow inside the chamber is turbulent to ensure the aerosol is well mixed radially and to minimize particle fallout along the length of the tube. The recirculating flow is HEPA filtered on each cycle to provide freshly generated aerosol and ensure that the PSD inside the optical viewing region is constant over time (i.e. eliminate cumulative effects of particle fallout). A window purge system keeps particles from accumulating on the windows, thereby minimizing optical scattering from the windows.
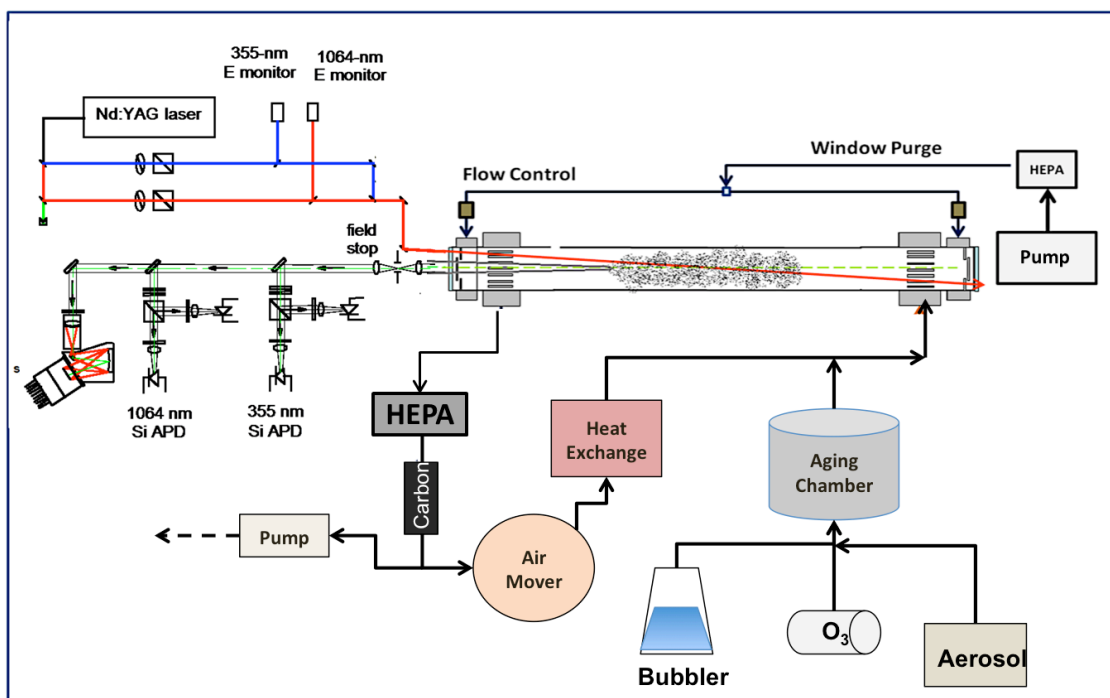
Figure 1. Schematic of constant flow aerosol chamber with circulation system and optical path through the chamber indicated.

Either dry or wet aerosol particles may be disseminated into the chemical reaction flow tube then injected directly to a turbulently mixed, constant-flow aerosol chamber (shown in Figure 1) and the aerosol optical properties may be measured with an optical system looking through the aerosol cloud**.** The aerosol chamber is constructed such that the recirculating flow is HEPA filtered to remove hazardous aerosol particles from the circulated flow and maintained at a constant, though not controlled, temperature and

humidity. An additional activated carbon filter downstream of the optical measurements removes the residual organic gases that are generated during the aerosol aging process. Temperature within the system is held constant by passing the recirculated airflow through a heat exchanger to remove excess heat buildup from the regenerative blower, resulting in a steady temperature between 75°F and 80°F. Relative humidity is dependent on the ambient humidity and generally falls below 30%. The temperature and relative humidity are recorded continuously during data runs.

The flow tube dimensions are roughly 15 cm in diameter and 250 cm in total length from end to end with the measurement portion (aerosol-in to aerosol-out) of the aerosol flow tube equal to roughly 200 cm in length. With these dimensions and a flow rate of 35 cfm (0.0165 m^3/sec), we have average velocities near 200 ft/s (61 m/s) with a Reynolds number value near 9000, so the requirement for turbulence to efficiently mix the aerosol throughout the measurement region is met. In turbulent flow, loss of particles >0.1 µm is predominantly by gravitational settling, with possible losses from turbophoresis at the higher Reynolds numbers and particle sizes in excess of 10 µm.

The design of the aerosol inlet plenum (right side of measurement tube according to the layout in Figure 1) provides a mechanism that efficiently mixes the aerosol population in the absence of turbulent flow. Within the inlet plenum, the aerosol laden flow is introduced into the flow tube using slots in a 360° pattern as illustrated in Figure 2. The exit plenum uses the same principle of operation, but works in combination with the Purge Air plenum to protect the window from contamination.
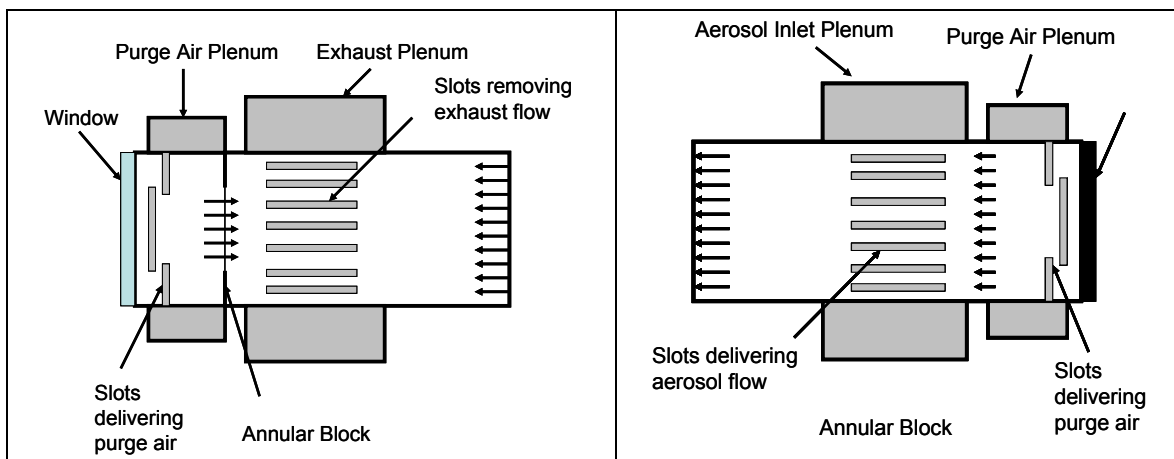
Figure 2. Schematic diagram for purge air deliver at the downstream (left) and upstream (right) ends of the flow tube, near the outlet and inlet plenums, respectively

To verify this initial mixing produces a uniform aerosol into the turbulent measurement region, flow simulation modeling was performed using SolidWorks Flow Simulation with a 100,000-point fine-mesh grid for particle trajectory analysis. Although there are limitations to SolidWorks Flow Simulation, as there are with any computational fluid dynamics model, it can accurately represent flows containing particles with similar

densities, no chemical reactions, and a single phase. As is outlined by (Matsson and Matsson 2012) results obtained with SolidWorks Flow Simulation are within 10% of the experimental results for three-dimensional fluid flow, so we can be confident that the results presented here are representative of the actual fluid flow within the system.

For particle trajectory modeling purposes, we use the particulate physical properties of Arizona Road Dust. Figure 3 shows the modeled particle trajectories for diameters ranging from 1 μm to 10 μm at a 50-cfm flow rate and standard temperature and pressure at the aerosol injection site. As is shown, the particles are directed around and through the inlet plenum, enhancing the turbulent mixing of the aerosol flow. These modeling results, coupled with the above referenced turbulent conditions, indicate that a well-mixed aerosol distribution will be maintained throughout the measurement region of the flow tube with minimal depositional and turbophoretic losses.
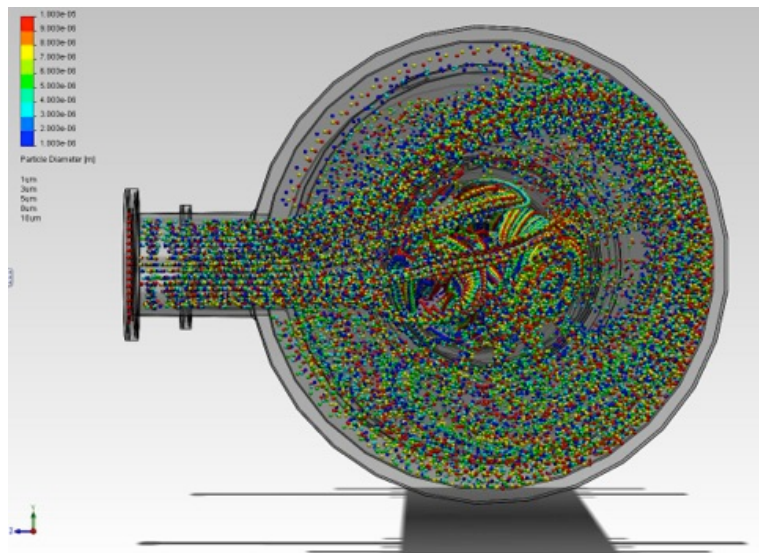
Figure 3. Modeling of the particle trajectories at the injection in the inlet plenum for different particle diameters.

Further verification of efficient particle mixing comes from direct particle size distribution measurements made within the measurement region of the chamber. To accomplish these measurements, samples of Arizona Road Dust (ARD) were drawn using the TSI Aerodynamic Particle Sizer (APS) at three interior positions within the chamber (1 inch, 3 inches, and 5 inches from the bottom) along the length of the viewing volume (seven preset sample ports roughly 22 cm apart). ARD was generated using the Fluidized Bed Aerosol Generator (FBAG). Figure 4 shows the resulting flow-tube radial and vertical aerosol distributions. As is depicted in Figure 4, regardless of position, the concentration remained around the average determined in the pre-measurement setup, with particles as large as 10 μm being transported the length of the flow tube. Much of the variation can be attributed to the standard variability using the FBAG and instrument uncertainty for the APS.
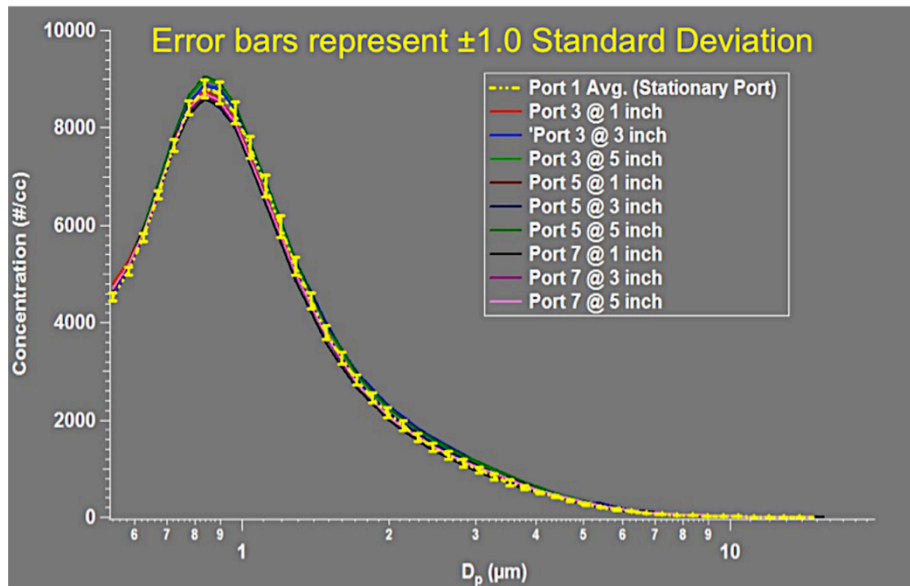
Figure 4. Measured ARD both axially and radially in the measurement region. The error bars represent +/- 1 standard deviation to the average of measurements at port 1 (the only stationary measurement port)

2.2. Bi-static LIDAR Optical System

This section describes the design and implementation of the optical system used to measure backscatter and laser induced fluorescence (LIF) cross sections as well as depolarization ratios at 355 nm and 1064 nm in the specially designed aerosol flow chamber. Since the aerosol cross section measurements are made in a relatively short chamber (~2 meters long) at quite short standoff (~1.5 meters to center of the aerosol cloud), a bistatic LIDAR arrangement (as shown in Figure 5) is advantageous because the recorded optical signals originate only from the geometrical overlap of the transmitted beam and the receiver field of view. Thus, we can design this region to be inside the aerosol flow chamber where the aerosol concentration and particle size distribution are uniform and known (measured). We can directly measure the region of overlap in a calibration procedure by translating a small spectralon target through the overlap region and measuring the optical system response. During the same calibration, we can relate each detector response to the others, allowing us to use the N_2 Raman signal as a cross section calibration. Moreover, the bistatic arrangement virtually eliminates the backscattered signal from the windows, which, in a coaxial LIDAR arrangement, could easily dominate the signal from the aerosols being measured.
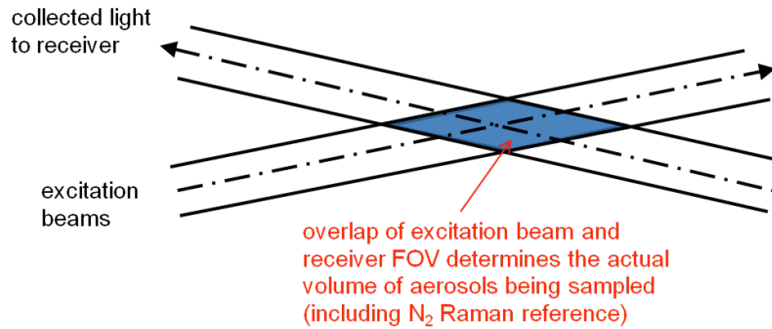
Figure 5. A bistatic LIDAR arrangement ensures that signals observed originate from the overlap region of the excitation beam and receiver field of view.

An optical schematic of the transmitter and receiver system is shown in Figure 6. A Big Sky model CFR-200 flashlamp-pumped Nd:YAG laser produces ~8-ns-long pulses at 1064 nm and 355 nm at 30-Hz repetition rate. These two wavelengths are separated and propagated along different paths so that the polarization state and energy of each can be independently controlled using a series of waveplates and polarizers. In addition, beamsplitters in each beamline are used to sample ~1% of each beam to send to an energy monitor. Once calibrated, these energy monitors continuously record the transmitted laser energy and are used for energy normalization in the data processing steps. Not shown in the figure is a 1:1 beam expander and loose spatial filter used on the 1064-nm leg to clean up its far-field spatial profile and reduce its beam size inside the chamber (slightly).
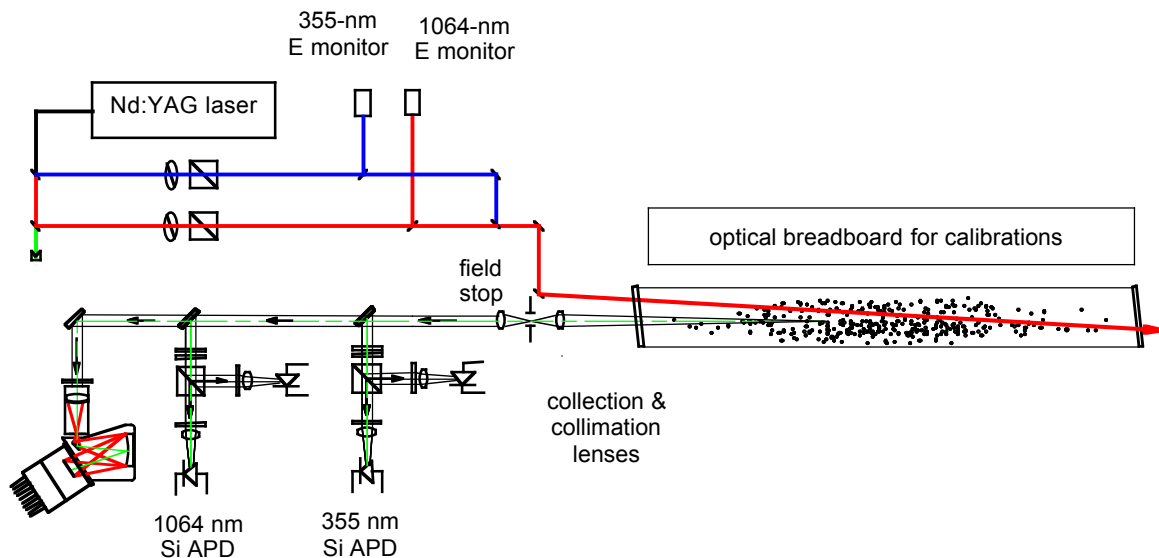
Figure 6. Optical schematic of the transmitter and receiver optical system

The 1064- and 355-nm beams are then combined to be collinear before they are transmitted into the chamber. Both beam diameters are nominally 6 mm and are linearly polarized in a plane oriented 45° from vertical. Although the receiver optics are designed to be polarization neutral (i.e. roughly the same reflectivity for s- and p-polarized light),

we orient the input laser polarization 45° from vertical to ensure there is no systematic bias for polarization due to the receiver optics. The input laser beams are transmitted into the chamber at angle of about 1° from the centerline of the chamber. The receiver field of view is oriented -1° off the chamber centerline so that the scattered light collected is only about 2° off true backscatter (180°). Thus, our measured cross sections can be considered backscatter cross sections (without any further corrections).

The receiver optical system is also shown in Figure 6. The backscatter and LIF signal collection optic is a 35-mm-dia. 120-mm focal length UV-grade fused silica lens. It is critical that this lens (and any of the optics following it that may feed the LIF channel) is fabricated from UV-grade fused silica because other materials will fluoresce and obscure the LIF signal from the aerosol under study. A second 35-mm-dia 120-mm focal length UV-grade fused silica lens is placed roughly 2f from the first collection lens to approximately collimate the collected backscatter and LIF photons. An adjustable iris (nominally set to 1 mm diameter) in between the two lenses serves as the field stop for the system.

As described before, the collected backscatter and LIF light is roughly collimated after the collection and collimation lens pair, and is transmitted to a set of three detector arms: one to detect polarization-resolved elastic backscatter at 355 nm, one to detect polarization-resolved elastic backscatter at 1064 nm, and one to detect spectrally resolved LIF excited at 355 nm. The beamsplitters used to feed the three detector arms are copies of those used in the B70 trailer LIDAR receiver. At 45° angle of incidence, the 355-nm pickoff reflects ~60% (unpolarized) of the 355-nm light and transmits >95% of the light from 380 – 700 nm. It also transmits >95% of the 1064-nm light incident. This beamsplitter design transmits a significant amount of 355-nm elastic light (~40%) to the ICCD/spectrograph for the hard-target calibration procedure and ensures that the N_2 Raman signal (at 386.67 nm) is not attenuated. The 1064-nm beamsplitter reflects >95% of the 1064 light (unpolarized) while transmitting the >95% of the light from 355 – 700 nm which is transmitted to the spectrometer/ICCD arm. Since the spectrometer/ICCD is the last detector arm in the series, a UV-enhanced Aluminum mirror is used to turn the beam.

A more detailed schematic of the polarization separation optics for the elastic backscatter arms is shown in Figure 7. First, a half-wave plate and quarter-wave plate pair are used to adjust the polarization state of the collected light to compensate for any ellipticity that may be induced by the mirrors, beamsplitters, and other optics feeding the detector arm (and to rotate the linear polarization axis 45° since the input polarization was rotated 45° with respect to vertical). During instrument setup and calibration (which will be described in more detail later) we adjust these waveplates to optimize the polarization discrimination for known linearly polarized inputs. After the waveplate pair, the collected light passes through a Glan laser polarizer (Karl Lambrecht model MGLS-SW-20), which separates the input beam into two output beams with orthogonal linear polarization states. Each leg (polarization state) passes through a 1:1 telescope with an iris that serves as a loose spatial filter. This spatial filter prevents the weak back-reflection of the transmitted (p-polarized) beam from contaminating the reflected (s-

polarized) signal, thereby ensuring maximum discrimination of the two polarization states. The polarizers have a clear aperture of 20 mm, an extinction ratio of $2x10^{-5}$, and an angular acceptance of $\geq 5°$ at 355 nm and $\geq 7°$ at 1064 nm.

The lenses forming the spatial filter are 25-mm dia. 50-mm focal length (nominal) plano convex lenses. After the spatial filter, the input (for each leg) is focused onto an avalanche photodiode (APD) using another 25-mm dia. 50-mm-fl (nominal) plano-convex lens. A narrow bandpass filter is used in front of each APD to eliminate cross talk between the 1064- and 355-nm channels.

The detectors used for the 355-nm elastic backscatter channels are Hamamatsu C-5331-11 Si avalanche photodiodes (APDs). On the 1064-nm channels, Hamamatsu C-53331-03 Si APDs are used. Both models have 1-mm-dia. active area and are operated at the factory preset gain ≈ 30. The -11 model is optimized for shorter wavelength operation as needed for the 355-nm detection. These APD detectors have on-board HV supplies and preamplifiers and the HV supply is temperature compensated to for < 2.5% change in gain for temperatures in the range of 25±10°C. Our laboratory temperature stays well within this nominal range.

The wavelength-resolved LIF detector channel consists of a Horiba CP-140-1605 imaging spectrograph with an Andor gated, intensified CCD (ICCD) in the back focal plane. The dispersion of the grating combined with 18-mm-dia Gen II photocathode allows spectrally resolved detection of light from ~350 nm to 640 nm. The grating is blazed for peak throughput at 450 nm. An Opto-Sigma model 027-3010 UV achromat is used to focus the input light onto the entrance slit of the spectrometer. Using a 250-micron-wide entrance slit, the measured spectral resolution is about 5.5 FWHM (measured using the linewidth of a tunable HeNe laser).
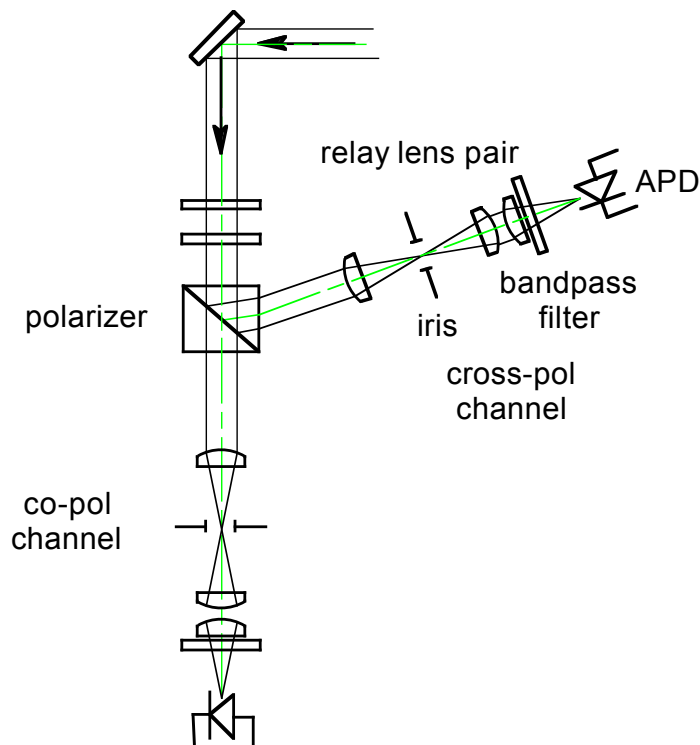
Figure 7. Detail of the polarization separation optics used for both the 355- and 1064-nm elastic backscatter channels. A loose spatial filter is used in each leg to ensure optimum polarization discrimination ratio. A bandpass filter is used ensure no cross-talk between channels.

During normal operation (i.e. while recording data on aerosols) a sharp-turn-on long-pass filter from Barr Associates is used to block the elastically scattered 355-nm light while allowing the fluorescence and Raman-shifted light to be transmitted. During the hard-target calibration procedure, the Barr filter is removed so that the 355-nm elastically scattered light can be recorded on the ICCD.

Figure 8 is a photo showing the optical test section of the BSL-1 aerosol chamber and an overall view of the optical system. The transmitter and receiver portions are separated by black foamcore partitions to prevent spurious scattered light from contaminating the signals. In fact, most of the light-proofing has been removed for the photo so that the components are visible. In operation, all of the individual detector legs have individual covers and baffles to reduce randomly scattered light signals and cross-talk between wavelength channels. Also, when in operation, light-proof covers are placed between the optical system and the entrance window of the aerosol chamber to further reduce light pollution and allow the system to be operated with the room lights on. (The ICCD detector is very sensitive and will record the spectrum of the room lights if the aforementioned cover is not in place.)
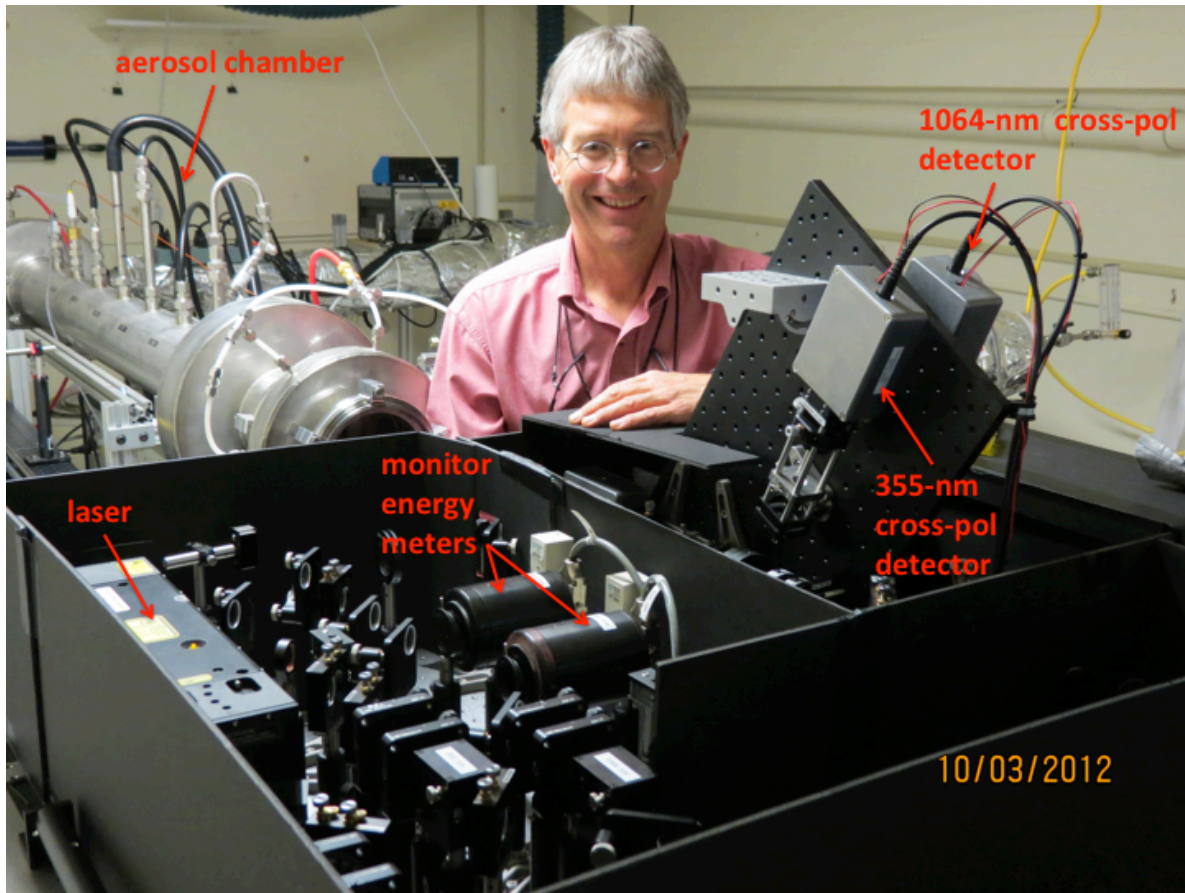
Figure 8. Photo of aerosol chamber and optical system.

At the far end of the optical measurement section of the aerosol chamber, a laser beam dump is installed inside the chamber to reduce scattered light from inside of the chamber. Even though the bistatic LIDAR arrangement minimizes the detected signal from the windows, if the input laser beams are not efficiently trapped, the secondary scatter from the windows and inside walls of the tube are big enough to dominate the scattered and fluorescent signal light from the aerosol. In addition to using a high-performance Black Hole laser beam dump at the terminal end of the optical measurement volume, we have found it beneficial to cover the inside of the exit window with high-performance, low-fluorescence black matte coating to reduce scattered light inside the tube even further. In addition to providing optimally low background scattered light inside the chamber, optically blocking the exit of the chamber and optically sealing the entrance of the chamber to the transmitter/receiver make the system a Class 1 laser system (no beams accessible), and, as a result, the operators do not have to wear laser protective eyewear. The exception to this is during maintenance and calibration, some of the covers are off and the laser beams transmit in free space so laser protective eyewear is needed for those short periods of time.

Figure 9 is a photo showing more detail on the 1064-nm elastic backscatter and wavelength resolved LIF detection channels. The 1064-nm received light path is outlined

in blue. It first passes through a half-wave plate and quarter-wave plate to orient the co- and cross-polarized components to be linearly polarized vertical (p) and horizontal (s) respectively. A Glan laser polarizer splits the input into two beams: the transmitted p-polarized beam is detected by the co-pol APD and the reflected s-polarized beam is detected by the cross-pol APD. These are mounted on small vertical breadboard to make the overall setup more compact. The 355-nm elastic backscatter detection system looks identical and is mounted on the back side of this breadboard. The beam path for the LIF detection channel is outlined in green. A lens mounted on the front of the CP-140 spectrograph focuses the input light onto the entrance slit of the spectrograph. A gated, intensified CCD (ICCD) mounted in the back focal plane of the spectrograph records the spectrum. During normal operation, a sharp turn-on low-pass optical interference filter is placed in front of the lens in front of the spectrograph. Also, neutral density filters (not shown) are used in all of the channels during hard-target (and other) calibrations to prevent detector saturation and/or damage due to high signal returns
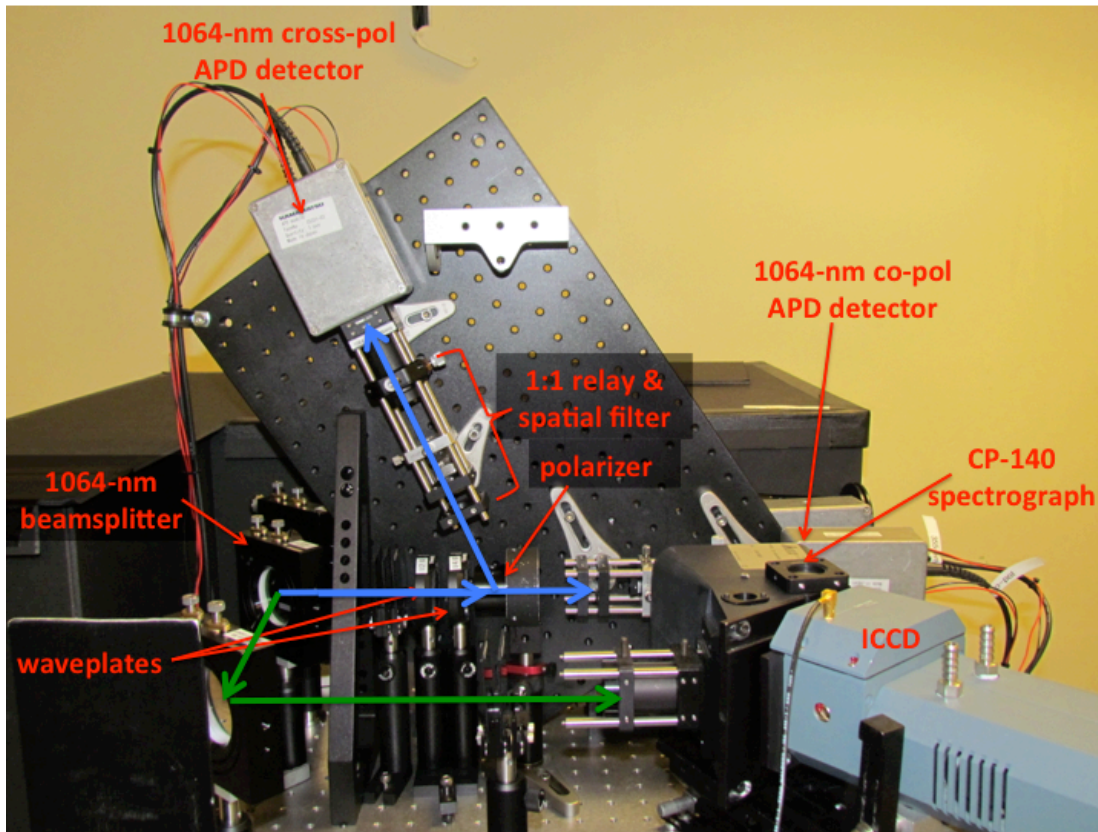
Figure 9. Photo of 1064-nm elastic backscatter leg and ICCD/spectrograph (LIF) leg.   The 1064-nm beamline is highlighted in blue. The LIF optical path is shown in green. The 355-nm elastic backscatter detection system is nominally identical to the 1064-nm leg and is on the back side of the angled breadboard.

The entire optical system, consisting of the transmitter and receiver shown in Figure 6, is mounted on a 36-inch-wide by 48-inch-long breadboard, which is in turn mounted on a stand in front of the aerosol chamber. The transmitter/receiver breadboard is mounted on a two-position linear bearing that allows it to be translated perpendicular to the axis of the

aerosol system (i.e. perpendicular to the transmitter/receiver optical axis). In one position, the transmitter/receiver is aligned along the axis of the aerosol system (looking into the chamber) for making aerosol cross section measurements. In the second position, the optical system is aligned to be parallel to the chamber, but with the laser beam and receiver field of view over an optical breadboard used for alignment, beam diagnostics, and calibration. In this alignment/calibration position, the laser beams are accessible so that their size, overlap, and other beam characteristics can be measured. In this position, a reference energy meter can be used to calibrate the pickoff energy meters on the optical system. The optical calibration breadboard also contains a ~2-m-long motorized translation stage used to translate a Spectralon target along the length of the aerosol chamber to perform the hard-target calibration procedure. Prior to making optical measurements on aerosols, a series of calibrations and system checks are performed to ensure data quality and collect the necessary data for absolute optical cross section computation.

A summary plot of a typical hard-target calibration is shown in Figure 10. Here we plot the normalized response of each detector as a function of distance along the chamber (or aerosol cloud region). The position $z = 0$ is the center of the chamber. The green cursors at $z = \pm60$ cm indicate the position of the extreme APS measurement locations. The aerosol between these locations is known to be well mixed and homogeneous. Note that the integrated response of all five-detector channels is largely within these bounds. The black dashed cursors at $z = \pm80$ cm indicate the position of the entrance and exit plenums. The response of all five detectors is essentially zero outside these bounds, as required for measuring reliable optical scattering cross sections.

Note that all five detector channel sensitivities peak near the center of the chamber and are essentially zero in regions where the aerosol concentration is not known to be uniform. The fact that the exact shape or peak position of all of the curves are not exactly coincident does not affect the accuracy or reliability of the resulting cross section measurements because the optical signal collected from an aerosol cloud (including the N_2 Raman from the air) is proportional to the integrated response (i.e. the integral of the calibration curve). It is important to look at these curves to make sure that the each detector's response looks reasonable (stable day to day, etc.) and is positioned to have essentially zero response outside the region where the aerosol concentration is known. For computation of the optical cross sections, we use the integral each detector's response over all z positions. The theoretical basis for the hard-target calibration as well as its use in computing cross sections is described in more detail in Appendix A. We measure one or more hard-target calibrations each day to track and account for optical alignment changes over time. In general we have found that the optical alignment remains relatively stable day-to-day and month-to-month. Moreover, the important quantity in the cross section calculation, the ratio of any detector's hard-target calibration to that of the ICCD, is even more stable over time because the primary source of alignment drift is the transmitted laser beam pointing, not the receiver alignment. Even though the hard-target calibration results are consistent day to day, we use the value measured on any given day to compute cross sections for that day's data. In this way, we account for small drift in the optical alignment, if it occurs.
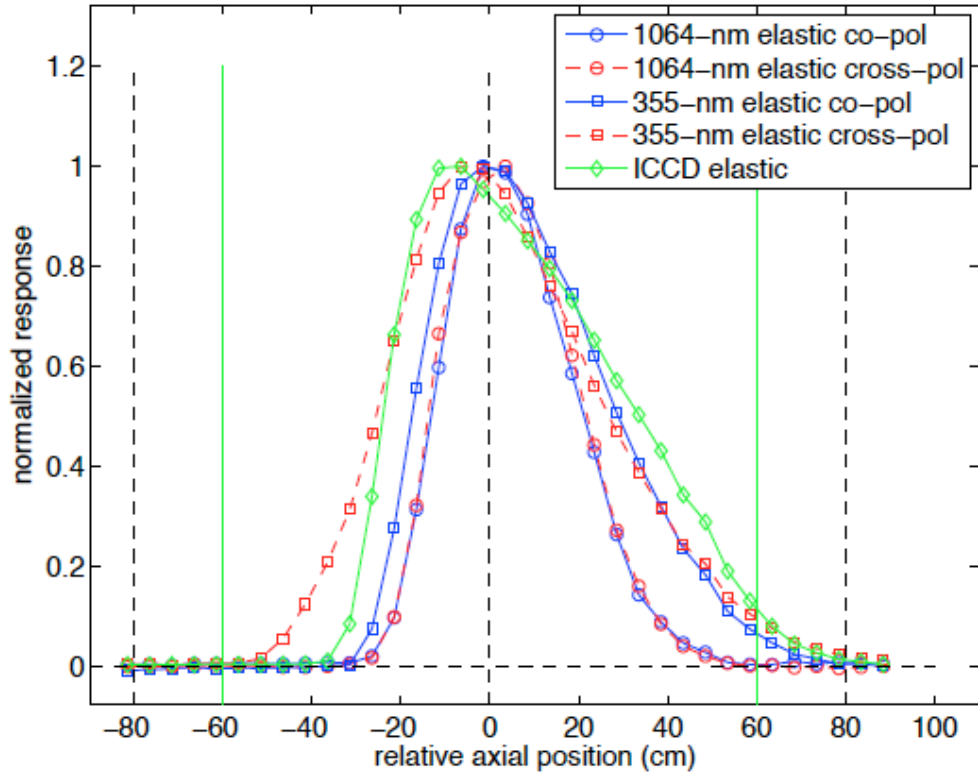
Figure 10. Typical hard-target calibration summary plot. Here we plot the normalized response of each detector as a function of distance along the chamber (or aerosol cloud). The position 0 is the center of the chamber. The green cursors at z = ±60 cm indicate the position of the extreme APS measurement locations. The aerosol between these locations is known to be well mixed and homogeneous. The black dashed cursors at z = ±80 cm indicate the position of the entrance and exit plenums.

Figure 11 shows an example of the clear-air N_2 Raman signal obtained from 30 laser shots (1 second) of ~8 mJ/shot at 355 nm. The Raman signal has very high signal-to-noise and the background LIF signal is quite low to permit aerosol cross section measurements with low uncertainty, perhaps as low as a calculated ±15%.

single 30-shot accumulation clear air signal
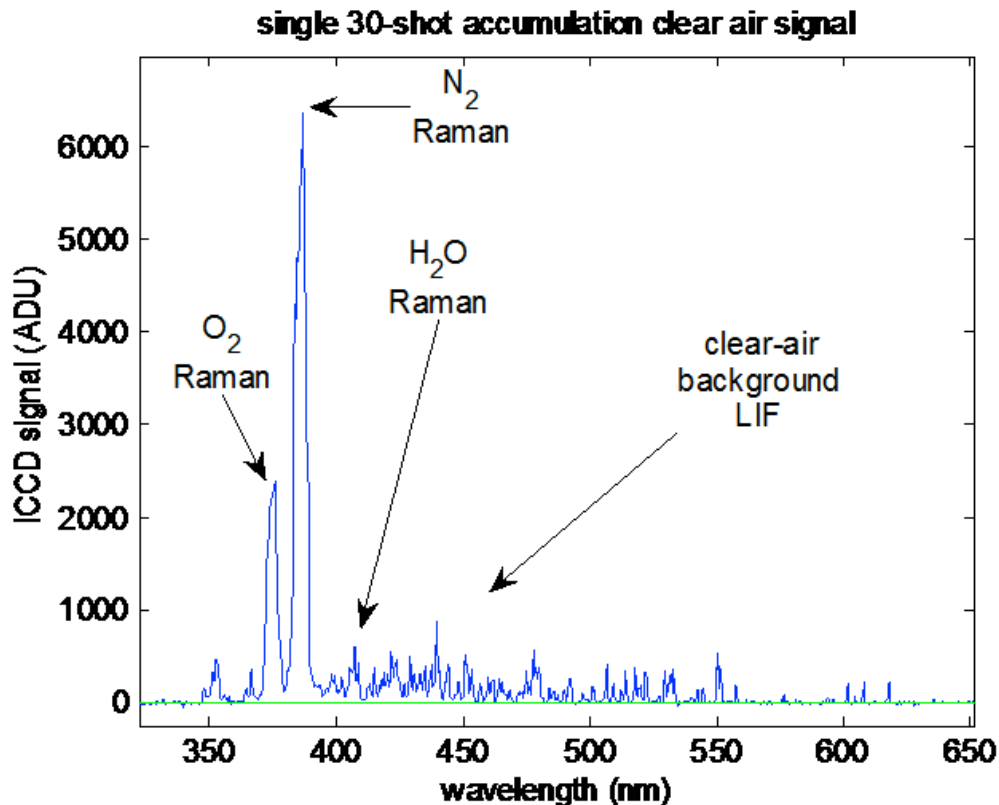
Figure 11. Measured clear air ICCD signal showing the intensity of the Nitrogen and Oxygen Raman peaks along with the measured clear-air background.

Each aerosol measurement period (or trial) consists of at least 5 minutes of measuring clear air signals followed by a minimum of 5 minutes measuring an aerosol release followed by another clear-air measurement period. This process is generally repeated for the same material between 2 and 4 times. Furthermore, each material trial is repeated on different days to enable any data outliers that may exist to be identified based on optical system response in the event that the optical system was not performing optimally on any given day.

An example showing the integrated 355-nm APD signal during a typical release cycle is shown in Figure 12. In this plot, the APS concentration is scaled to match the co-pol signal and tracks it very well except during extreme aerosol concentration transients that occur when the dissemination device is turned on. Concentration spikes are often observed during a release period and are due to the initial startup of the aerosol generation device. These transient spikes aid in time syncing between the aerosol measurements and the optic signals.
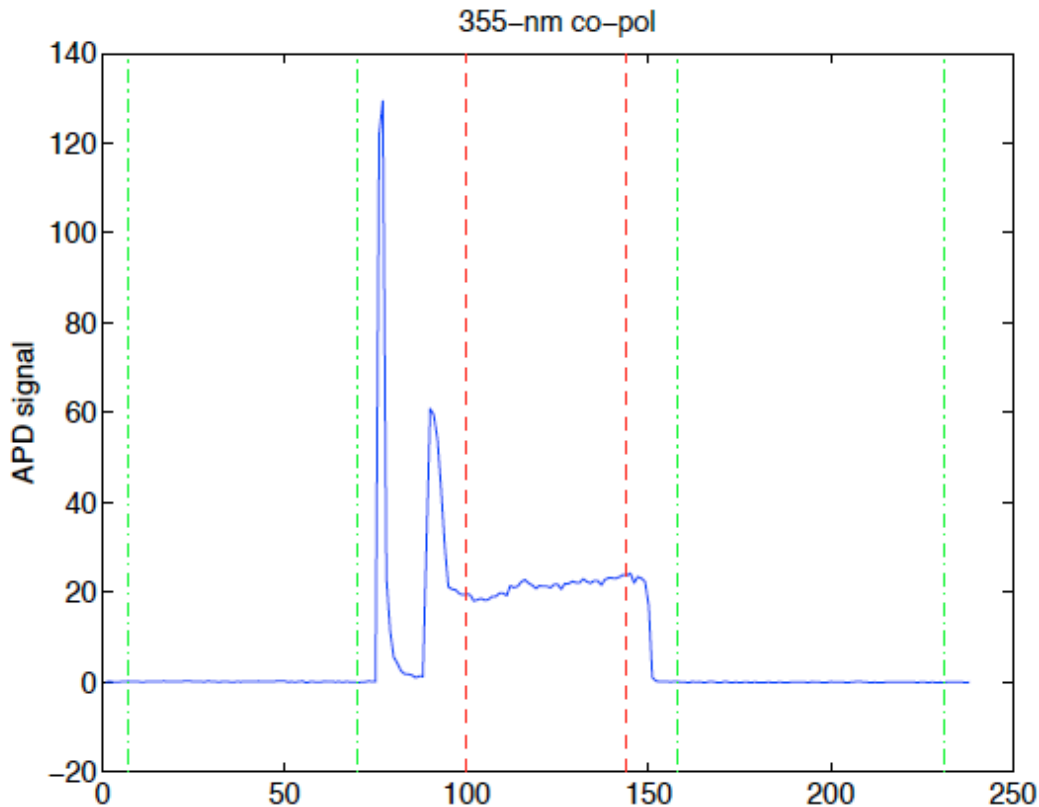
Figure 12. Example showing a single release period showing the identified clear air regions, aerosol startup concentration spike, and measured stable aerosol cloud.

The signals occurring between the green cursors are the clear air periods before and after the aerosol release while the signals occurring between the magenta cursors contain the aerosol cloud data that will be processed to compute cross sections. Note that we exclude regions with extreme concentration transients and select regions where the aerosol concentration and PSD is relatively stable over time.

As mentioned previously, the optical backscatter and LIF cross sections are computed on 6-sec time intervals that match the APS readings. The cross sections we report are the average cross section during a single cloud period. The uncertainty in the cross section for each cloud is reported as the standard deviation of the optical cross section values during each cloud period. Sometimes this method overestimates the uncertainty. For example, if the fluctuations in concentration are significant during the cloud period and if the time synchronization of the optical and APS readings are not perfect, then the reported cross section will have high standard deviation even though the overall signal to noise ratio of the measurement is very high. Averaged over a 4- or 5-minute long cloud period, the effect of these deviations will average out and the average cross section value should be of high confidence.

The atmospheric aerosols we are studying (NaCl, KCl, Ammonium Nitrate, Ammonium Sulfate, laboratory-grade black carbon and Arizona Road Dust) do not exhibit fluorescence emission due to their material composition – i.e. they do not contain

24

aromatic fluorophores usually responsible for fluorescence. Due to this fact, the LIF cross sections measured in this study were below the noise limit of the system, and no LIF measurements will be presented in this report. For consistency, and to help determine if the optical measurement system is performing optimally, backscatter cross section measurements of commercial Btk were obtained at the beginning of each measurement day.

2.3. Chemical Flow Reactor for Aerosol Aging

The aerosol chemical flow reactor developed specifically for this study is shown in Figure 13. It was fabricated from 6-inch diameter stainless steel vacuum tube with bent sections and straight sections welded together in a helix so that 37 linear feet of tubing occupies only about $1m^3$ of laboratory space. This helical chemical flow reactor has over 205 liters of chemical reaction volume.   In order to prevent material degradation from the harsh chemicals, the entire flow system is made of brushed stainless steel and pressure leak tested at both +5 and -5 psi deviation from atmospheric. Chemical flow reactors have been used in numerous studies to quickly react products in flowing environment (Pfeiffer, Forberich et al. 1998, Czoschke, Jang et al. 2003, Jang, Lee et al. 2003). Contrary to the more traditional static smog chamber approaches (Wang, Paulson et al. 1992), a chemical flow reaction method allows for a constant and steady aerosol flow environment. This method enables the coupled aerosol flow and optical LIDAR system to obtain data over long periods of time thereby improving the backscatter cross-section measurement.
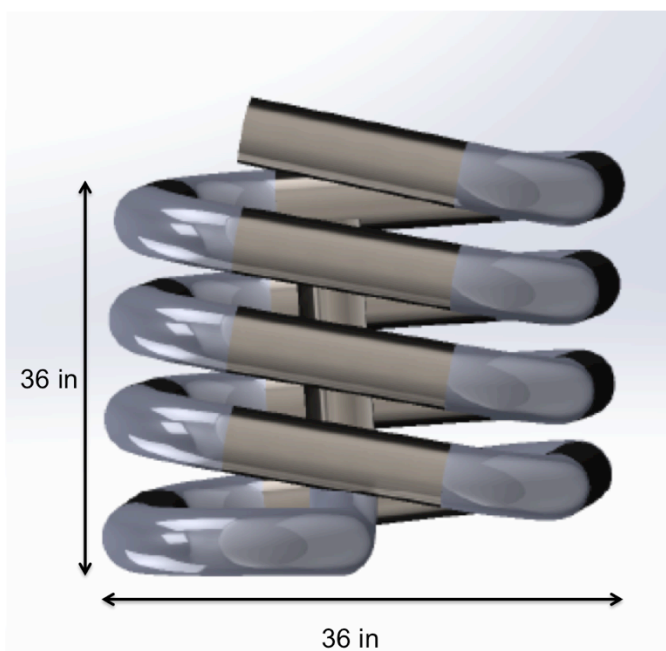
Figure 13. Solidworks representation of chemical flow reactor

A schematic showing the flow path of the chemical/aerosol mixture is given in Figure 14. For optical measurements of the pure aerosol experiencing no chemical aging, the pure

aerosol was mixed with filtered dry laboratory grade compressed air instead of the chemical aging agent. Similarly, when atmospheric aerosols were aged using pure H_2SO_4 vapors, the H_2SO_4 stream from the bubbler was mixed with pure laboratory-grade compressed air. The H_2SO_4 bath was also heated to provide more efficient transfer to the vapor phase. H_2SO_4 production in the atmosphere accounts for a large fraction of secondary aerosol formation (Hitchcock, Spiller et al. 1980). H_2SO_4, formed by the oxidation of SO_2 in the presence of water molecules, is an indirect product of coal and gas combustion as well as oil refining (Rodhe, Crutzen et al. 1981). DMS is also a source of SO_2 in marine atmospheres. During each aerosol aging and non-aging experimental setup, the flow rate through the chemical flow reactor was set to a total of 10 lpm, which results in a roughly 20 minute residence time prior to injection into the optical LIDAR measurement system.
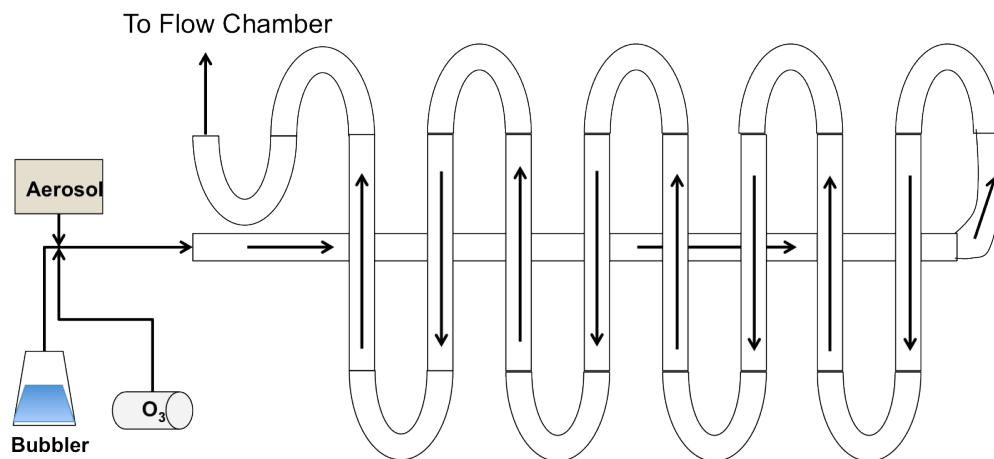
Figure 14. Chemical flow reactor flow schematic. Flow through the chamber is set at a constant 10 lpm allowing for a 20 minute mixture residence time.

When aging aerosol with toluene and m-xylene ozonolysis reactions, O_3 was mixed with toluene in the reaction chamber with no addition of dry, filtered compressed air. O_3 was generated using a flow cavity generation Mercury vapor discharge lamp operating at near 185 nm peak wavelengths. The O_3 generation cavity was a specially designed hollow Teflon housing with a 2 inch ID and roughly 5 inches in length, which worked to contain the Hg vapor lamp and allow for dry, filtered compressed air to pass through being exposed to the ultraviolet radiation source. The oxygen present in the compressed air is quickly photolyzed by the wavelength output of the Hg lamp leading to the generation of excited oxygen molecules. These excited molecules react within seconds with an additional oxygen molecule leading to measured O_3 concentrations within the flow chamber near 500 ppb. While these concentrations are significantly above urban ambient values, the desired elevated concentrations are intended to represent local and regional plume concentrations following immediate emission. The elevated O_3 concentration also ensures the ozonolysis of both toluene and m-xylene despite the limited residence time within the flow chamber (Pfeiffer, Forberich et al. 1998, Czoschke, Jang et al. 2003).

Both toluene and m-xylene are a class of aromatic hydrocarbons that react readily with O_3 through ozonolysis to produce methyl-glyoxal and glyoxal bi-products (Finlayson-Pitts and Pitts 1997, Bahreini, Keywood et al. 2005, Bloss, Wagner et al. 2005). While the pathways leading to organic aerosol formation remain highly uncertain (Hallquist, Wenger et al. 2009), it is estimated that the SOA production from toluene could account for a large fraction of atmospheric organic loading (Shapiro, Szprengiel et al. 2009). Both m-xylene and toluene are more reactive with O_3 and other oxidizing agents than their benzene precursors due to the addition of methyl groups (one for toluene and two for m-xylene) (Suh, Zhang et al. 2003, Baltaretu, Lichtman et al. 2008). Toluene is produced from both biogenic mechanisms, through pine oil, and industrial processes such as the crude oil refinery process (Zhao, Hopke et al. 2004, Buzcu and Fraser 2006). A sizable fraction of the global toluene budget can also be attributed to combustion of gasoline. Toluene is the most abundant aromatic hydrocarbon in the atmosphere (Finlayson-Pitts and Pitts 1997, Hurley, Sokolov et al. 2001, Hallquist, Wenger et al. 2009, Shapiro, Szprengiel et al. 2009). Though lower in atmospheric concentration, m-xylene is also a bi-product of industrial processes and manufacturing as well as combustion of oil and gas. The hydrocarbons selected for this study therefore represent secondary organic precursors found in petrochemical refinery and other industrial manufacturing plumes (Kleinman, Daum et al. 2002, Ryerson, Trainer et al. 2003, Zhao, Hopke et al. 2004). For the purposes of this study and understanding the secondary organic aerosol formation from coal burning power plants, H_2SO_4 and $(NH_4)_2SO_4$ aerosol are most representative due to the aerosol forming potential SO_2 emitted from coal combustion and other manufacturing processes in the presence of ammonia, a commonly known indirect emission factor.

To provide reference (non-aged) aerosol, the neat (pure) aerosol types were injected through the chemical flow reactor in the absence of chemicals. With a 20-minute residence time and a flow rate of only 10 lpm, particle populations injected into the 37-feet of stainless steel tubing will experience depositional losses, thereby altering the originally disseminated distribution. This method allows for pure aerosol to undergo the same depositional losses as the aged aerosol resulting in the ability to directly compare the measured optical properties. Of the aerosols studied, black carbon and Arizona Road Dust were generated using a CH Technologies, Inc. Vilnius Aerosol Generation system whereas aerosol disseminated in solution, $(NH_4)_2SO_4$, NH_4NO_3, NaCl, and KCl, were generated using the Sono-tek ultrasonic nozzle.

For aerosol populations that were chemically aged, the methodology required the establishment of chemical mixing within the flow reactor prior to introducing particles into the stream. This ensures that the pure aerosol is exposed to the chemical aging environment for the full 20-minute residence time. Following transition through the chemical flow reactor, the aerosol is injected directly into the aerosol flow chamber and optical backscatter signals for both 355-nm and 1064-nm obtained using the bi-static LIDAR detailed in Section 2.2. Bi-static LIDAR Optical System. The backscatter energies recorded from the aerosol population are then processed to obtain the aerosol optical backscatter cross section and depolarization ratio.

2.4. Optical Cross Section Data Processing

We start with a simplified LIDAR equation for the signal produced by one of the detectors in the BSL-1 setup. The signal, S, from an optical receiver channel is given by

$$S = E_L \frac{A}{R^2} T(\lambda_{laser}) T(\lambda_{signal}) \varepsilon_{laser} \varepsilon_{signal} \Delta L \frac{d\sigma}{d\Omega} N_{total} \qquad \text{(Eqn. 1)}$$

where

E_L is the energy of the transmitted laser pulse,

A is the area of the receiver aperture,

R is the range to the cloud,

$T(\lambda)$ is the transmission of the atmosphere at wavelength λ,

ε_{laser} is the optical transmission efficiency of the transmitter optics (input window of chamber),

ε_{signal} is the optical system transmission efficiency (including the loss of the window and any electronic gain) of the receiver optical system,

ΔL is the length of the cloud measured,

$\frac{d\sigma}{d\Omega}$ is the scattering cross section, and

N_{total} is the number density of the aerosol for all size bins of interest (usually $1 - 10$ μm).

Because the distance to the cloud is only a few meters and for 355nm $\leq \lambda \leq 1064$ nm, the transmission of the atmosphere may be set to 1 for both the laser and the signal wavelengths. The efficiency factor for the transmitted laser beam, ε_{laser}, is not constant with wavelength since the transmission of the AR coating on the entrance window has significantly different transmission at 355 than 1064 nm. (In addition, it will vary between cloud measurement and calibration where the window is absent). The window transmission vs. wavelength will also be a factor in the parameter ε_{signal}.

In our system, the effective length of the cloud measured, ΔL, is determined by the transmitter/receiver field of view overlap angle and the size of the laser beams. Also, the solid angle of signal light collected, $\frac{A}{R^2}$, changes significantly throughout the measurement volume. A hard-target calibration will be used to determine the value of the combined factor $\mathbb{C} = \frac{A}{R^2} \Delta L \varepsilon_{signal}$, which is the optical throughput, integrated over the entire measurement volume. We end up with a general equation for the response of a generic optical receiver channel:

$$S = E_L \varepsilon_{laser} \frac{A}{R^2} \Delta L \, \varepsilon_{signal} \frac{d\sigma}{d\Omega} N_{total} \qquad \text{(Eqn. 2)}$$

or

$$S = E_L \varepsilon_{laser} \mathbb{C} \frac{d\sigma}{d\Omega} N_{total} \qquad \text{(Eqn. 3)}$$

It will be convenient to normalize the detected signal by the laser energy. If we define the normalized signal as

$$S' = \frac{S}{E_L} \quad \text{, the basic BSL-1 LIDAR equation becomes}$$

$$S' = \varepsilon_{laser} \mathbb{C} \frac{d\sigma}{d\Omega} N_{total} . \qquad \text{(Eqn. 4)}$$

Calibration of one optical channel with respect to the others is accomplished by translating a spectralon target through the measurement volume and recording the system response as a function of distance from the receiver. The signal from the hard target may

be written as: $S'_{HT} = \varepsilon_{laser} \frac{A}{R^2} \varepsilon_{signal} \rho^*$ where the factor ρ^*, the hard target reflectivity,

replaces the factor $\Delta L \frac{d\sigma}{d\Omega} N_{total}$ in the normal (aerosol version of the) LIDAR equation.

(Note that the value of ρ^* can be equal to ρ, $\frac{\rho}{\pi}$, or even $\frac{\rho \cos(\theta)}{\pi}$ depending on the

angular scattering properties of the hard target[1]. Since the Spectralon target we use is a

good Lambertian scattering surface, $\rho^* = \frac{\rho}{\pi}$, where ρ is the reflectivity of the target.

For all practical purposes, $\rho \approx 1$ for all wavelengths we use in the current BSL-1 work,
355nm $\leq \lambda \leq$ 1064 nm.)

In the hard-target calibration, we want determine the net (or effective) value of

$\mathbb{C} = \frac{A}{R^2} \Delta L \varepsilon_{signal}$ over the entire measurement volume.

During the hard target calibration, we measure the hard-target return signal at a number of axial locations starting with regions where the optical system response is negligible, going through maximum responsivity, and ending at a position with negligible sensitivity. An example of a normalized hard target calibration is shown in Figure 15 below.

The factor $\mathbb{C}$ is the area under the curve normalized by the laser energy. In the case of measurements at discrete z locations, we can write

$$\mathbb{C} = \sum_{\substack{cal \\ z_i}} \varepsilon_{signal} \frac{A}{R^2} \rho^* \Delta z \qquad \text{(Eqn. 5)}$$

Note that we are not attempting to absolutely radiometrically calibrate any of the receiver channels. We only need to calibrate them relative to one another and, in the end, we will ratio everything to the N_2 Raman signal.

We can write the N_2 Raman signal as

$$S'_{Raman} = \varepsilon_L \mathbb{C}_{Raman} \frac{d\sigma}{d\Omega}_{Raman} N_{N_2} \qquad \text{(Eqn. 6)}$$

where N_{N_2} is the number density of N$_2$ molecules in the air and $\dfrac{d\sigma}{d\Omega}_{Raman}$ is the N$_2$ Raman cross section.
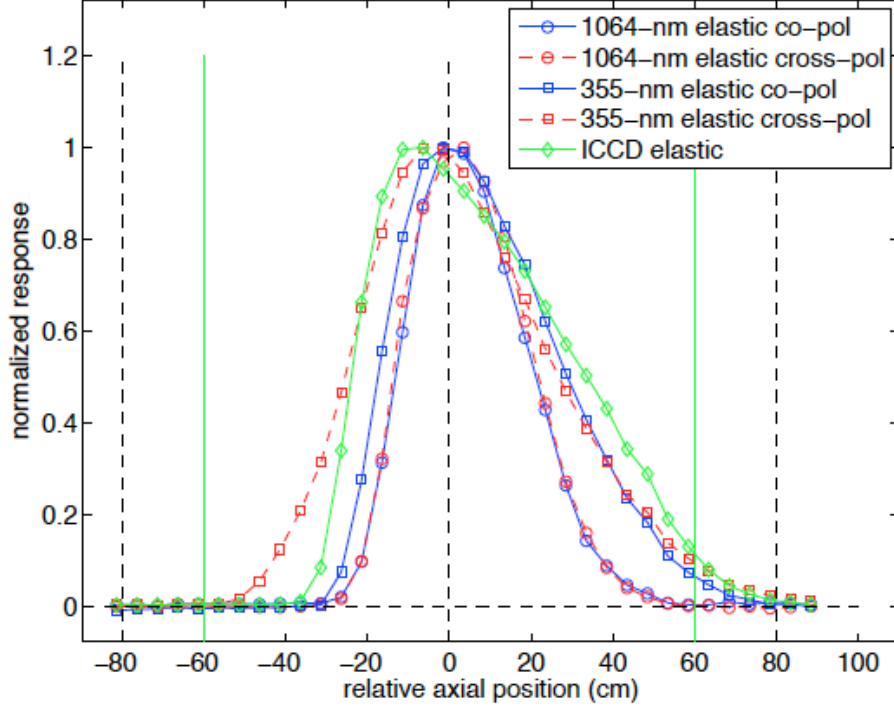
Figure 15. Example of hard target calibration data for all five detector channels: 1064-nm elastic (co- and cross-polarized), 355-nm elastic (co- and cross-polarized), and ICCD elastic. The data is normalized to show that the response of the system turns on and turns off as expected and that the response of all of the wavelengths is in essentially the same spatial region.

Likewise, we can write the 1064-nm elastic backscatter signal as

$$S'_{1064\,back} = \varepsilon_L \, \mathbb{C}_{1064\,back} \, \frac{d\sigma}{d\Omega}_{1064\,back} \, N_{total} \,. \qquad \text{(Eqn. 7)}$$

To find the 1064-nm backscatter cross section, we divide one equation by the other to obtain

$$\frac{d\sigma}{d\Omega}_{1064\,back} = \frac{S'_{1064\,back}}{S'_{N_2 Raman}} \frac{\varepsilon_{L355}}{\varepsilon_{L1064}} \frac{\mathbb{C}_{N_2 Raman}}{\mathbb{C}_{1064\,back}} \frac{d\sigma}{d\Omega}_{N_2 Raman} \frac{N_{N_2}}{N_{total}} \qquad \text{(Eqn. 8)}$$

where ε_{L355} and ε_{L1064} are the laser transmission efficiencies for the N$_2$ Raman channel and 1064-nm channel respectively. Note that each channel will, in general, have a different calibration factor $\mathbb{C}$.

The 355-nm backscatter and laser induced fluorescence (LIF) channels are special cases since the laser transmission efficiency of the system is the same. Thus for 355-nm backscatter, we can write

$$\frac{d\sigma}{d\Omega}_{355\,back} = \frac{S'_{355\,back}}{S'_{N_2 Raman}} \frac{\mathbb{C}_{N_2 Raman}}{\mathbb{C}_{355\,back}} \frac{d\sigma}{d\Omega}_{N_2 Raman} \frac{N_{N_2}}{N_{total}} \,. \qquad \text{(Eqn. 9)}$$

Likewise, for the LIF channel we can write

$$\frac{d\sigma}{d\Omega}_{LIF} = \frac{S'_{LIF}}{S'_{N_2 Raman}} \frac{\mathbb{C}_{N_2 Raman}}{\mathbb{C}_{LIF}} \frac{d\sigma}{d\Omega}_{N_2 Raman} \frac{N_{N_2}}{N_{total}} \,. \qquad \text{(Eqn. 10)}$$

It is worth reminding ourselves that the calibration-determined constant $\mathbb{C}$ is a function of wavelength. The calibration factors $\mathbb{C}_{N_2 Raman}$ and $\mathbb{C}_{LIF}$ are determined from 355-nm elastic backscatter measured on the ICCD and the standard lamp calibration which corrects for the wavelength-dependent sensitivity of the ICCD/spectrograph and the longpass (Barr) filter used to block the 355-nm elastic during normal operation.

To determine the signal return from N_2 Raman scattering, we calculate the N_2 concentration as 79% of the gas concentration of normal air and use the ideal gas law:

$$N_{N_2} = 0.79 \times \frac{P}{kT} \qquad \text{(Eqn. 11)}$$

At standard temperature and pressure, $N_{N_2} = 1.9 \times 10^{25} m^{-3} = 1.9 \times 10^{19} cm^{-3}$. When analyzing the experimental data from the LIDAR system, we compute the nitrogen concentration based on the measured temperature and pressure inside the aerosol chamber during the measurements.

The total N_2 vibrational Raman scattering cross section is calculated from the measurement by Inaba, (Inaba and Kobayasi 1972), who measured a cross section of 3.5×10^{-30} cm^2/sr/molecule at a laser wavelength of 331.7 nm, corresponding to a laser photon energy of 30,148 cm^{-1}. The Raman scattering shift for N_2 is 2331 cm^{-1}. Because the Raman scattering cross section scales inversely as the Raman scattered wavelength to the fourth power, the total N_2 vibrational Raman scattering cross section resulting from a 354.7-nm laser (corresponding to a photon energy of 28,193 cm^{-1}) is

$$\frac{d\sigma_{N_2 Raman}}{d\Omega} = 3.5 \times 10^{-30} \left(\frac{28193 - 2331}{30148 - 2331} \right)^4 cm^2 / sr / molecule \qquad \text{(Eqn. 12)}$$
$$= 2.6 \times 10^{-30} cm^2 / sr / molocule \,.$$

The depolarization ratio, δ, is usually defined (in this report) as the ratio of the perpendicularly polarized backscatter cross section to the total backscatter cross section:

$$\delta = \frac{\sigma_\perp}{\sigma_\perp + \sigma_P}$$

(Eqn. 13)

The cross section data processing is implemented in Matlab, and will not be described in this report except in general terms. The Matlab code reads the raw data files from the data acquisition computer, the APS, and an auxiliary data acquisition card (the chamber temperature, pressure, and flowrate). For each data run, the analysis code plots both the optical response and the measured aerosol concentration vs. time, and, through a graphical user interface, allows the user to define the clear air periods and aerosol cloud periods for each data run.

Clear air periods are those times before and after an aerosol release where the concentration of aerosol inside the chamber is essentially zero (because of the HEPA filtration in the air circulation loop). The clear air periods are used to define baselines for each of the detectors and compute the noise of the system (i.e. the variability in the detector response in the absence of aerosol). In addition, the magnitude of the N_2 Raman signal is determined during clear air periods to avoid contamination with the laser induced fluorescence signal (for those aerosols with a fluorescence response).

Cloud periods are those intervals where the aerosol concentration (and other experimental parameters) are stable (in terms of aerosol concentration and particle size distribution) so that reliable backscatter cross sections can be computed. Choosing a period in the cloud where the conditions are stable is particularly important for the aging study. One must identify where the chemical reactions (aging) has reached a steady state. The backscatter and LIF cross sections for the aerosol under study are computed using the equations outlined above. The Matlab data analysis programs also store the data and intermediate computations so that they can be easily summarized in excel spreadsheets, plots, and the like.

3. RESULTS AND DISCUSSION

3.1. Measured LIDAR Backscatter Cross sections

The total measured elastic backscatter cross section for all pure particles are presented in Figure 16. As described in Section 2.2, the (temporal) portion of the cloud used to compute cross sections is selected manually (using a Matlab gui) to ensure that extreme particle concentration fluctuations due to aerosol generator start-up transients and other anomalies are not included in the cross section computation. The cloud release time can vary slightly from one release to the next, but is typically about 5 minutes long, with a minimum 3 minutes of steady-state aerosol cloud where the aerosol concentration and particle size distribution do not vary significantly over time.

To first order, variations in aerosol concentration and laser output energy are accounted for in the cross section calculation because the aerosol concentration and laser energy are recorded throughout the optical data collection period. The optical cross sections are computed at 6-second intervals (the data interval for the APS) for the duration of each cloud, and a simple measure of the uncertainty in the computed cross section for a given cloud is the standard deviation of the 6-second cross section values over the entire ~5-minute-long cloud period. The error bars shown in Figure 16 were computed as the standard deviation of the measurements for each cloud as described above. Included in this error bar are variations in cross section due to changes in the particle size distribution over the (temporal) length of the cloud. As mentioned before, in both the design of the instrumentation and the execution of the measurements, we aimed to maintain a stable aerosol concentration and particle size distribution to avoid these errors.

Occasionally, there are significant aerosol concentration fluctuations (or oscillations) during the cloud data acquisition periods. In these cases, if the time synchronization of the APS data and the optical data are not perfect, the standard deviation of the cross section values over the time of the cloud may be an overly pessimistic estimate of the data uncertainty (quality). That is, the mean value of the cross section will still be reliable (correct), in spite of the relatively high standard deviation of these measurements over time (due to a measurement and computational artifact). We have not yet derived an alternative method (based on signal-to-noise ratios or other independent factors) to measure the uncertainty in the cross section values.

The total elastic backscatter cross section for an aerosol is dependent on the size of the particles and their real and imaginary indices of refraction. Larger particles and/or larger real indices of refraction result in larger backscatter cross section. A larger value of the imaginary index of refraction (which is responsible for optical absorption) will result in lower backscatter cross section. Immediately evident in Figure 16 are optical scattering cross section groupings that emerge based on general pure particle type with the exception of a few obvious outliers. These groupings are salts, dust, and organic aerosol.
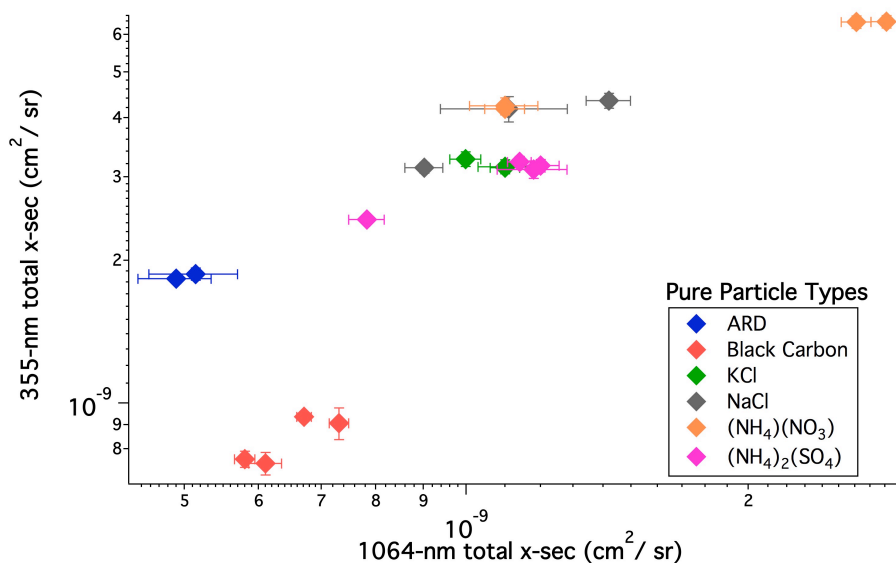
Figure 16. Total measured scattering cross section for pure particle types. General groupings are observed for salts, dust, and black carbon.

One material which does not appear to produce consistent measurements of backscatter cross section is ammonium nitrate. NH_4NO_3, a crystalline solid, did not show good repeatability in optical scattering cross section measurements, but does exhibit relatively large scattering cross sections. These results are likely due to the inconsistent clusters that form during NH_4NO_3 generation methods in solution. This can be seen in the aerosol size distribution inconsistency shown in Figure 17. The size distributions reported in Figure 17 are normalized to the maximum measured concentration to allow for easy visual comparisons. For polydisperse aerosols with particle sizes $\geq$ the measurement wavelength, the backscatter cross section scales roughly as the total area of the particles in the cloud (all other factors held constant) (Kovalev and Eichinger). As a result, one can see that shifts in the particle size distribution to larger particles can cause a disproportionate increase in measured cross section (since the contribution of each particle scales as the square of its diameter).

The salts measured show consistent cross section results with 355-nm scattering cross sections around 3.5×10^{-9} and 1064-nm scattering cross section value near 1.2×10^{-9}. Black carbon exhibited the smallest measured scattering cross section likely due to a large absorption of incident light, which is consistent with previous studies of the scattering properties of black carbon (Menon, Hansen et al. 2002, Andreae and Gelencsér 2006). The black carbon used for this study is laboratory grade fine powder black carbon purchased from Sigma Aldrich Corporation and was not freshly generated by combustion processes.

34
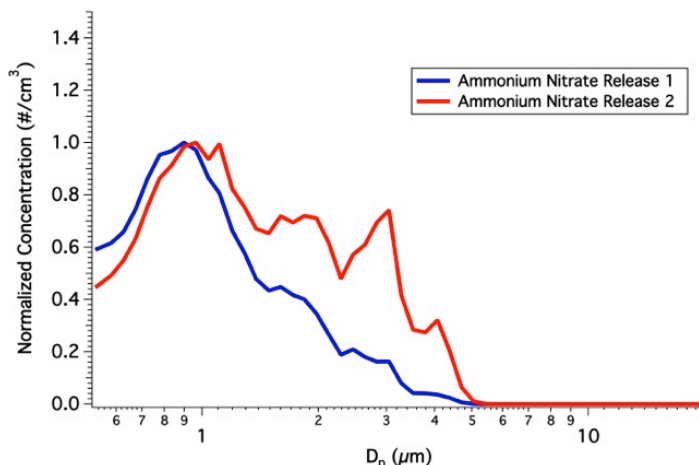
Figure 17. Average normalized measured size distributions for two ammonium nitrate releases that resulted in very different scattering cross sections.

The resulting measured total scattering cross section for 355-nm and 1064-nm wavelengths are given in Figure 18 for all particle mixtures with $(NH_4)_2SO_4$. In general, pure $(NH_4)_2SO_4$ particles scatter at 355-nm similar to their aged equivalents with values near 3.0×10^{-9} cm^2/sr. Most of the differences in scattering cross section are observed at 1064 nm. With the exception of a few outliers, all aging mechanisms decrease the 1064-nm scattering cross section with a H_2SO_4 coating leading to a reduction by as much as 50%. Despite the observed decreases in the 1064-nm optical backscatter cross section, a wavelength more sensitive to changes in PSD for particles sized 1 micron (wavelength ≈ particle size) or larger, the measured PSD for all cases remained fairly consistent as shown in Figure 19.
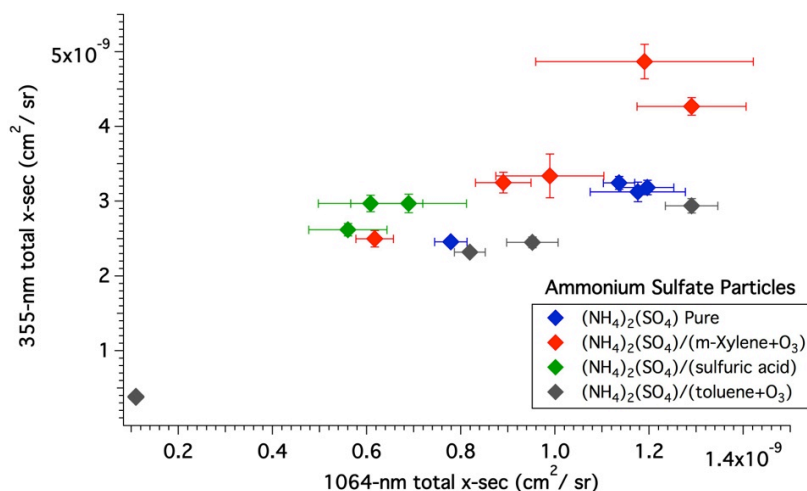
Figure 18. Total measured scattering cross section for ammonium sulfate particles.

As the $(NH_4)_2SO_4$ particles are aged by both toluene/ozone and m-xylene/ ozone mixtures, the size distribution shifts slightly to larger sizes supporting the reactive uptake

35

of glyoxal products during the aerosol aging process. While this increase is not observed in the overall size distribution for H_2SO_4-aged $(NH_4)_2SO_4$ particles, a more distinctive tail to larger sizes is evident in Figure 19 as well. The reactive uptake of low-volatility gaseous species onto $(NH_4)_2SO_4$ particles does result in a larger absorption cross section at 1064-nm. These results show that for $(NH_4)_2SO_4$, an overall increase in warming will be seen because of atmospheric aging when exposed to both anthropogenic and natural environments.
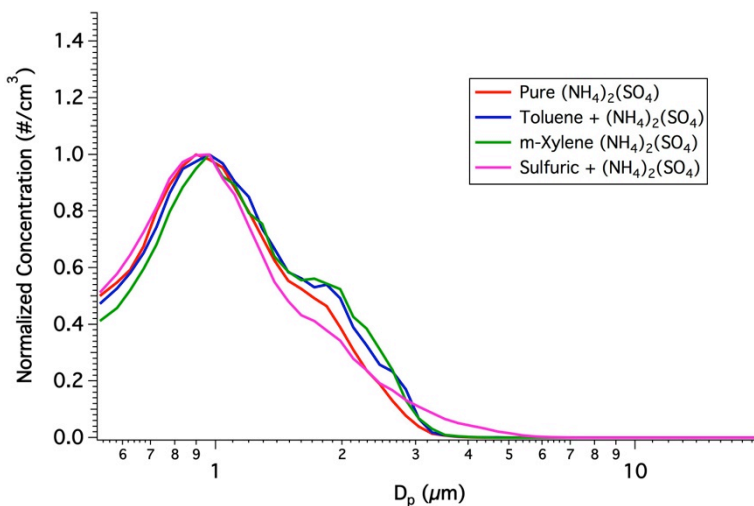
Figure 19. Measured average aerosol size distribution representative of all ammonium sulfate particle measurements, both pure release and aged.

Measured total scattering cross sections at 355 nm and 1064 nm are presented in Figure 20 for all cases of NH_4NO_3 particles studied. The two distinctly different scattering cross sections measured for pure NH_4NO_3 are due to drastic differences in the disseminated PSD as discussed previously. For the purposes of discussion, we will focus on the smaller of the two measured size distributions, which result in cluster of data that exhibit the lower of the two scattering cross section values. The values for pure NH_4NO_3 used here are 4.2 x 10^{-9} cm^2/sr at 355-nm and 1.1 x 10^{-9} cm^2/sr at 1064-nm. As shown in Figure 20, when NH_4NO_3 particles are aged by both H_2SO_4 and oxidized toluene, a decrease in backscattering cross section is observed, presumably due to an increase in the optical absorption. Up to a 90% reduction in both the 355-nm and 1064-nm scattering cross section values were observed during this study for NH_4NO_3 particles aged by glyoxal products resulting from the toluene oxidation by O_3. Similarly, a nearly 80% reduction in scattering cross section was observed when these particles uptake H_2SO_4. Consequently, in some cases, the reactive uptake of oxidized m-xylene products leads to an increase in scattering cross section.

36
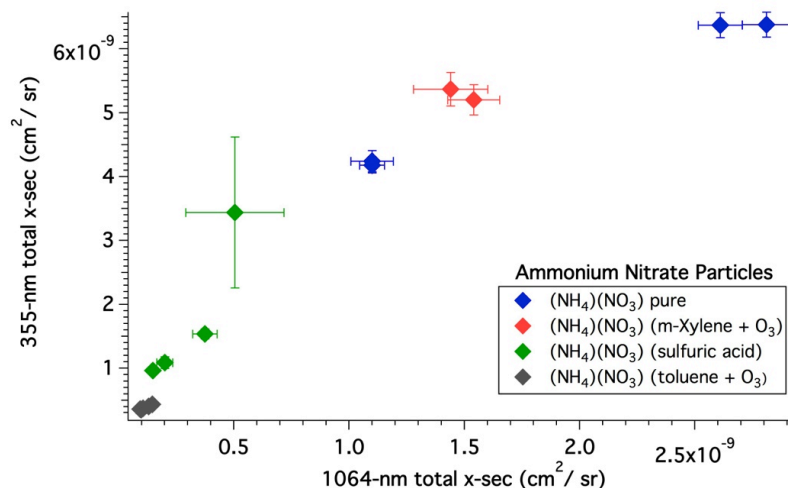
Figure 20. Total measured scattering cross section for ammonium nitrate particles.

Representative measured average size distributions for all measured NH_4NO_3 particles, both pure and aged, are given in Figure 21. For the purposes of discussion and consistency with the previous discussion, we will focus on size distribution comparisons of aged material with the pure distribution (solid red curve) in Figure 21. When NH_4NO_3 is aged by H_2SO_4 surface deposition, the resulting PSD measured was generally smaller in peak diameter. This decrease in size will affect the measured scattering cross section for the cloud somewhat, but since the scattering is proportional to the square of the diameter, this does not likely explain an 80% reduction in measured total cross section. Further investigation is required to better quantify the observed measurements with respect to PSD.
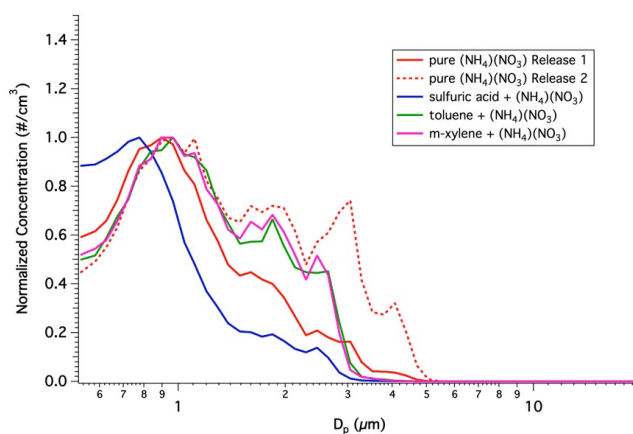
Figure 21. Measured average size distribution representative of all ammonium nitrate particle measurements, both pure and aged. Release 1 (red solid line) is representative of the lower measured pure particle cross section cluster in Figure 20; release 2 (red dashed line) is representative of the higher measured cross section.

The resulting PSD measured when NH_4NO_3 particles were aged by the products of toluene and m-xylene oxidation is larger in both peak diameter and across the majority of APS size bins larger than 1 micron. Despite the larger measured PSD, reactive uptake of toluene oxidation products still leads to a near 90% decrease in scattering cross section supporting the statement that these particles will absorb light more efficiently across all wavelengths and likely lead to a larger warming effect in the atmosphere. The same cannot be definitively stated for particles aged by m-xylene because of the lack of consistent pure particle size distributions. M-xylene-aged NH_4NO_3 particles scatter more efficiently when compared to the smaller of the two measured pure size distributions, but significantly less than the larger PSD.

For all aging processes involving NaCl studied, a decrease in total scattering cross section for both 355-nm and 1064-nm wavelengths was observed as shown in Figure 22. In addition to the previously presented H_2SO_4 aging discussions with $(NH_4)_2SO_4$ and NH_4NO_3, both NaCl and KCl were aged using a non-heated H_2SO_4 bubbler to supply vapors to the aerosol mixture. This was to help determine the effect of increased H_2SO_4 concentrations on optical scattering properties. As indicated in Figure 22, the heated H_2SO_4 bath resulted in a near 70% reduction in scattering cross section for both wavelengths whereas the non-heated H_2SO_4 bath resulted in only a 30% reduction. When comparing the size distributions in Figure 23, all aging methods resulted in a slightly smaller size distribution, The smaller size distribution seen when NaCl is aged by H_2SO_4 could be a result of the following: 1. the aerosol population is growing larger within the aging chamber causing a subsequent increase in deposition prior to measurement, 2. the uptake of H_2SO_4 leads to a higher wall loss coefficient within the aging chamber, or 3. the smaller sized particles are a result of sulfuric acid aerosol nucleation and growth mixing with the injected aerosol (Rodhe, Crutzen et al. 1981). While the timescale within the aging chamber does not support the presence of large H_2SO_4 aerosol, further testing is required to rule this effect null. The data indicates that reactive uptake of all chemicals studied by NaCl result in a decrease in scattering cross section and, as result, could lead to a subsequent warming effect. Results showing the decrease scattering cross-section for organic uptake by NaCl are consistent with previous studies investigating the absorption properties of SOA (Shapiro, Szprengiel et al. 2009, Zhang, Lin et al. 2011).
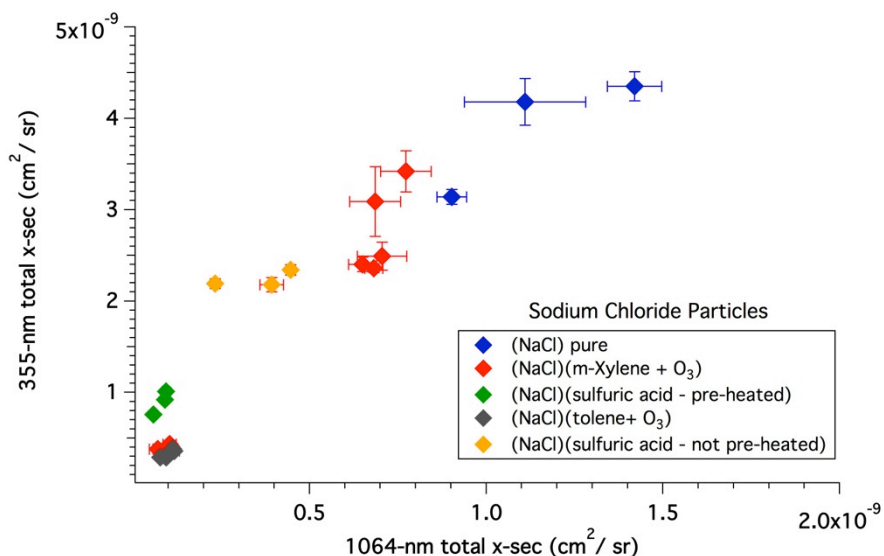
Figure 22. Total measured scattering cross section for sodium chloride particles.
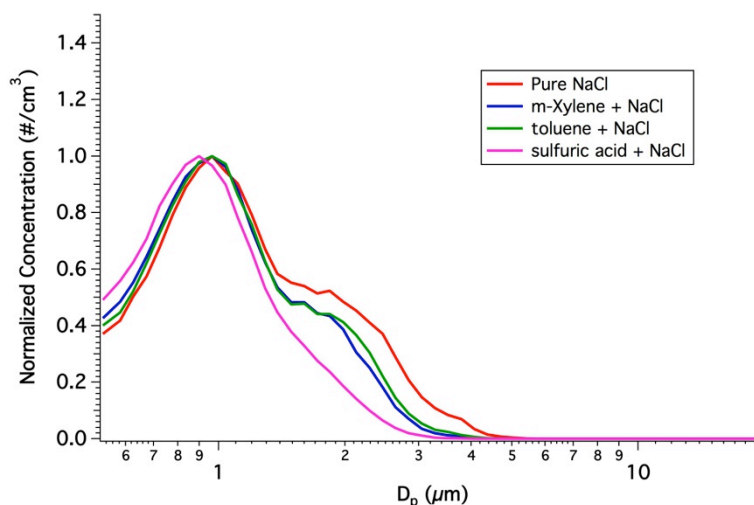
Figure 23. Measured average size distribution representative of all sodium chloride particle measurements, both pure and aged.

Results from trials involving KCl particles are presented in Figure 24, total scattering cross sections for 355-nm and 1064-nm, and Figure 25, measured particle size distributions. With the exception of the KCl aging by m-xylene oxidation, a general decrease in scattering cross section was observed for both wavelengths. Interestingly, the majority of m-xylene trials resulted in a roughly 10% increase in cross section despite a measured smaller size distribution as shown in the blue line in Figure 25. Similarly to that observed when comparing cross sections for NaCl particles aged by H_2SO_4, the heated bath resulted in a greater decrease in backscatter cross section over the non-heated bath. Reactive uptake of toluene oxidation products by KCl produced the largest decrease in scattering cross section of near 90% for 1064 nm and 95% for 355 nm. The measured PSD for KCl aged by toluene oxidation products also shifts to slightly larger

sizes, which would, when comparing pure KCl cross section at PSD to another, result in a larger cross section. Instead, a large decrease in scattering cross section is observed.
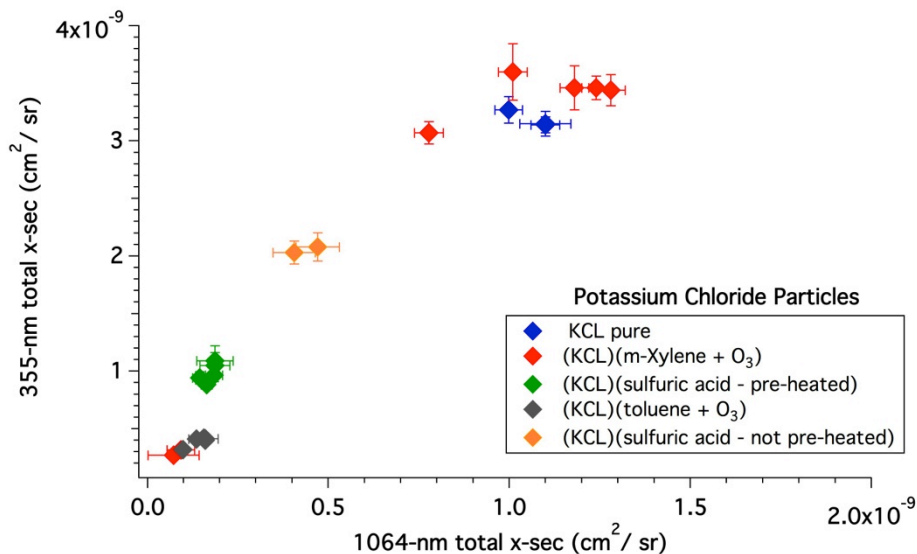
Figure 24. Total measured scattering cross section for potassium chloride particles.
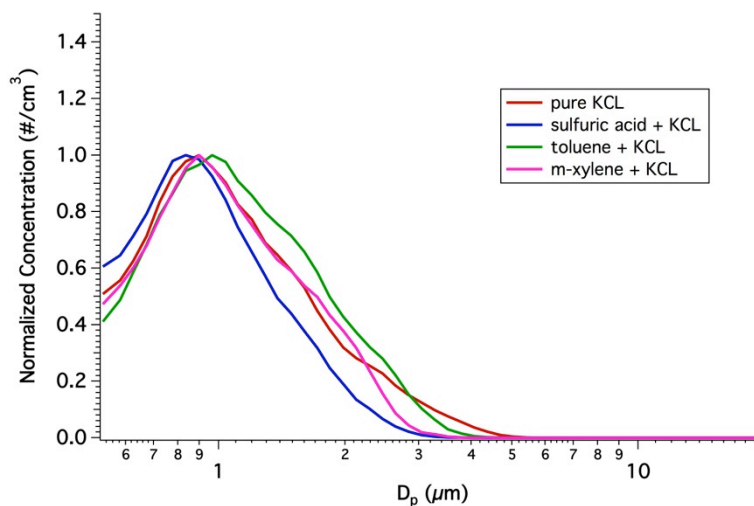
Figure 25. Measured average size distribution representative of all potassium chloride particle measurements, both pure and aged.

Black carbon aerosol exhibit lower scattering cross sections for the wavelengths studied when compared to the other atmospheric aerosol as is evident in Figure 26. These results are consistent with the assumption that black carbon has a higher absorption coefficient (Menon, Hansen et al. 2002, Andreae and Gelencsér 2006). The measured scattering cross sections are on the order of 8×10^{-10} cm^2/sr. When aged by H_2SO_4 deposition, black carbon becomes more efficient at scattering both 355-nm and 1064-nm light. Upon reactive uptake of oxidation products from toluene and m-xylene ozonolysis, black carbon aerosols absorb 355-nm and 1064-nm light more efficiently. These results are

supported by the measured representative size distributions reported in Figure 27, where little change to the aerosol PSD is observed. Based on the lack of size change evident in the disseminated black carbon aerosol from the differing aging mechanisms, changes in size distribution are not contributing significantly to the measured changes in cross section results presented in Figure 26, and all reported cross sections are specific to the aerosol mixing state with the aging chemical.
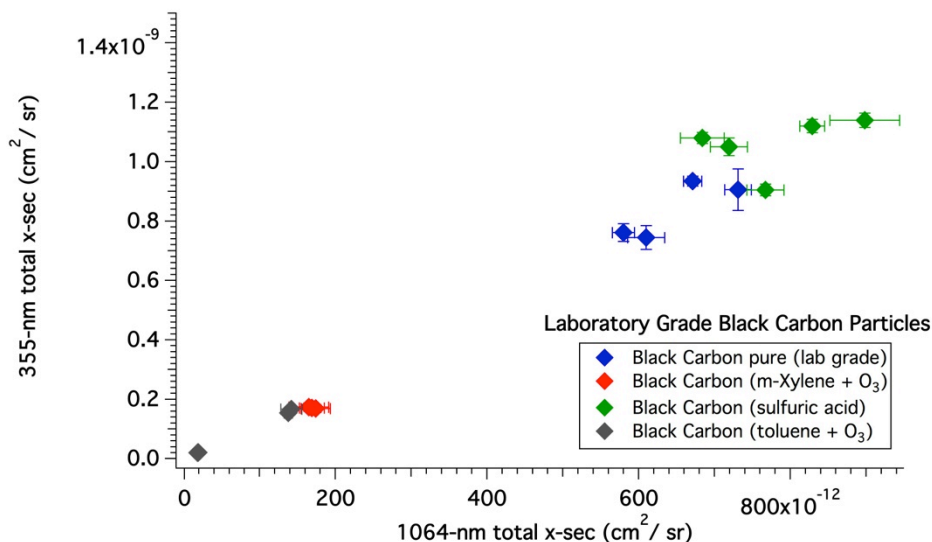
Figure 26. Total measured scattering cross section for black carbon particles.
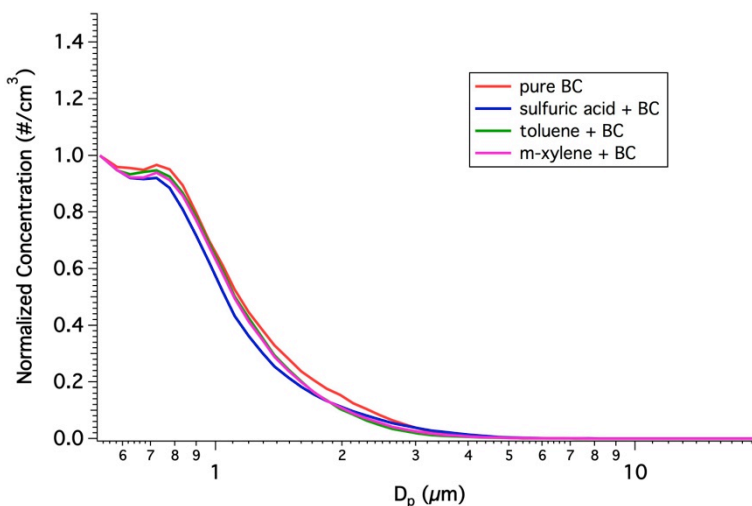
Figure 27. Measured average size distribution representative of black carbon particle measurements, both pure and aged.

Arizona road dust particles exhibit the most consistent surface interaction with the chemical aging mechanisms studied as shown in Figure 28. In all cases studied, the strong scattering signatures measured for pure Arizona road dust were decreased due to chemical aging.
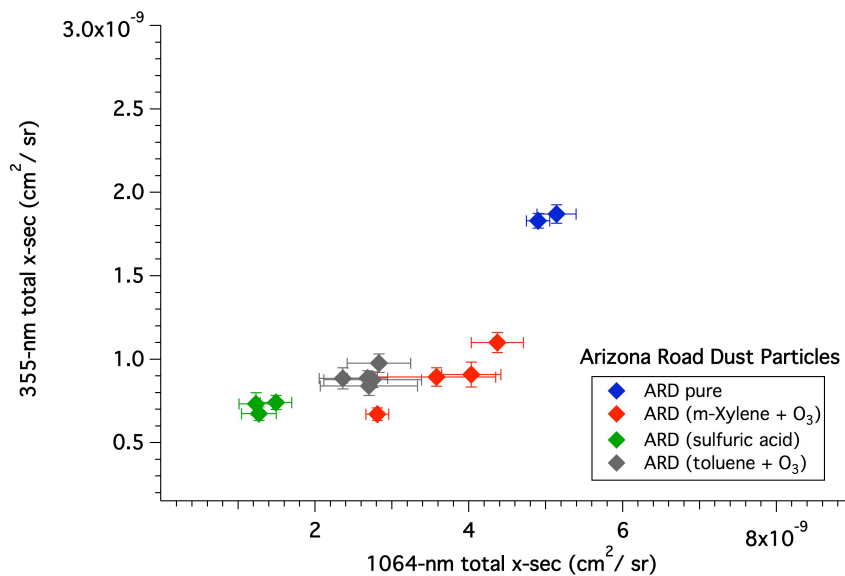
Figure 28. Total measured scattering cross section for ARD particles.

The largest decrease in scattering cross section was observed when ARD was aged using H_2SO_4 deposition. However, as presented in Figure 29, the measured aerosol size distribution was significantly smaller than pure ARD. When comparing the original, pure ARD size distribution to the PSD's measured for external mixtures of ARD with both toluene and m-xylene oxidation byproducts, there is little observable difference, although toluene aging does lead to slightly larger PSD's. In each organic aging case presented in Figure 28, a significant decrease in 355-nm scattering cross section was observed, with close to 60% reduction measured. The chemical aging of ARD also reduces the optical scattering of 1064-nm light by nearly 40%. These values are not well represented in global dust transport models. Because of the limited dataset, further investigation into the effect of organic coating on atmospherically relevant dusts is needed.
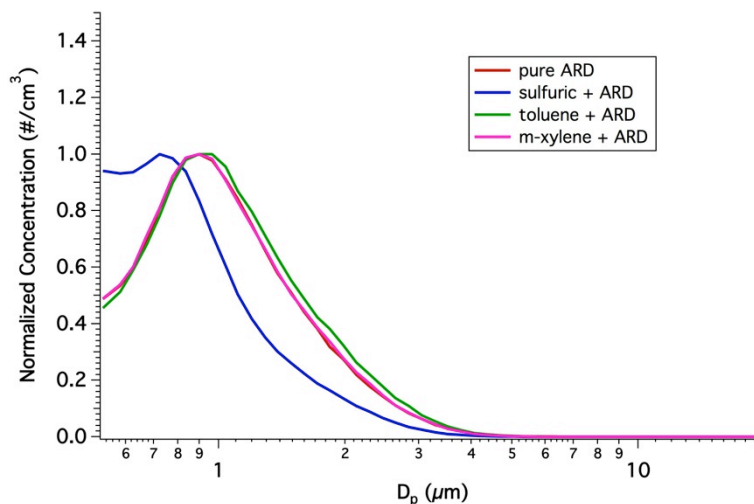
Figure 29. Measured average size distribution representative of all Arizona road dust particle measurements, both pure and aged.

A summary of optical scattering cross section results is present in Figure 30 for pure particles (top left), particles aged by H_2SO_4 deposition (top right), by toluene oxidation by O_3 (bottom left), and by m-xylene oxidation by O_3 (bottom right). All plots are scaled identically for comparison purposes. On average, $(NH_4)_2SO_4$ and NH_4NO_3 exhibit the least comparable decrease in scattering cross section when aged by H_2SO_4 and m-xylene oxidation products, though m-xylene-aged NH_4NO_3 scatters more efficiently. Little comparable change in scattering cross section is observed for toluene-aged $(NH_4)_2SO_4$.

Aging of KCl, NaCl, black carbon and ARD by all mechanisms studied results in decreased 355-nm and 1064-nm scattering cross section suggesting that these particles become more absorptive, which is consistent with recent studies (Shapiro, Szprengiel et al. 2009, Zhang, Lin et al. 2011). Interestingly, when toluene and m-xylene oxidation products age these particle types, they scatter less efficiently than pure black carbon aerosol, a result that has potentially large impacts to arctic climate in particular for considerations of dust transport across the pacific from Asia. Toluene-aged NH_4NO_3 also results in large decreases in the optical scattering cross sections at both wavelengths. Furthermore, the clustering of data points for these particle types following organic aging suggest that the oxidation products from both m-xylene and toluene ozonolysis dominate.
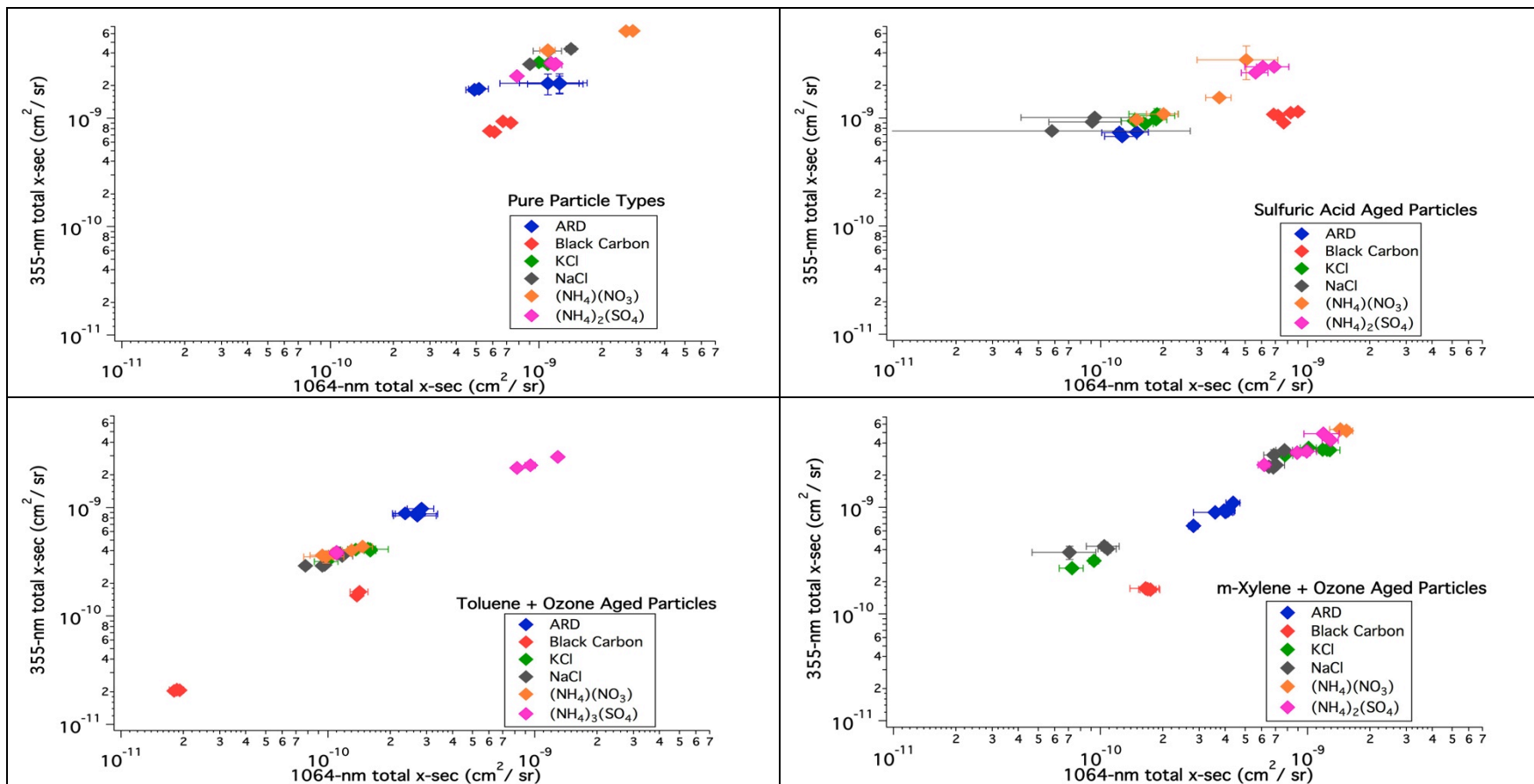
Figure 30. Comparison of total measured scattering cross section for pure particle types and all aging mechanisms. Log-log plots show the 355-nm backscatter cross section vs. the 1064-nm backscatter cross section. All axes are to scale.

3.2. Measured LIDAR Depolarization Ratios

As stated previously, the measured backscatter depolarization ratio is the ratio of the perpendicularly polarized component of the optical scattering cross section to the total optical scattering cross section: $\delta = \dfrac{\sigma_\perp}{\sigma_\perp + \sigma_P}$. Fundamentally, the depolarization of backscattered light is associated with the shape of the particles. Spherical particles do not depolarize the scattered light while asymmetrically shaped particles do. The magnitude of the depolarization ratio is a measure of the asymmetry (or departure from spherical shape) of the particles in an aerosol.

The measured depolarization ratio for each of the seven pure aerosol studied is presented in Figure 31. Similar to what was observed for the scattering cross section scatter plots, some groupings emerge. The groupings observed are primarily due to the shape of the measured aerosol, with NH_4NO_3 and the laboratory grade black carbon having the least irregular, and thereby more spherical structures. NH_4NO_3 and black carbon have depolarization ratios near 0.1 for 355-nm and near 0 for 1064-nm. NaCl and ARD exhibit similar shape factors with 355-nm and 1064-nm depolarization ratios near 0.3. KCl aerosol also show strong shape factors with depolarization ratios of 0.3 at 355-nm and 0.25 at 1064-nm.
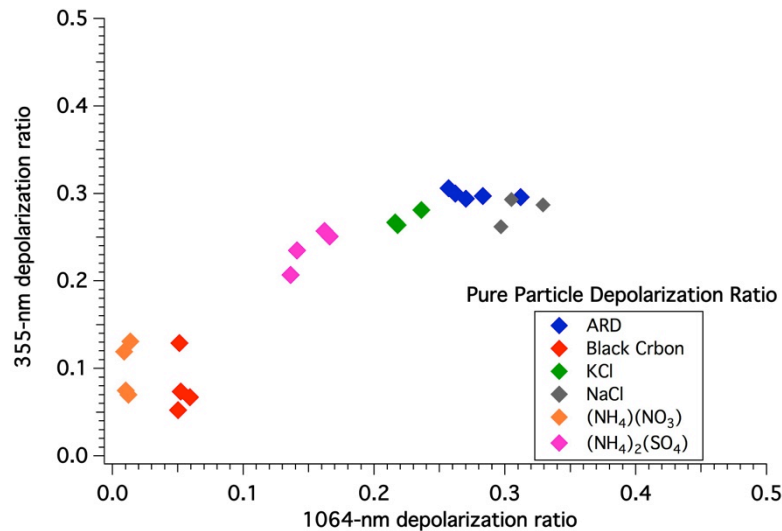
Figure 31. Measured optical backscatter depolarization ratio for 355-nm and 1064-nm. Evidence of more distinct groupings emerges when compared with optical backscatter cross section.

The results of measured depolarization ratios for pure and aged materials are given in Figure 32 for each individual particle type. Based on the traditional model for reactive uptake of organic and inorganic vapors and previously presented results of the measured scattering cross section, one would expect to see an overall decrease in depolarization ratio as particles age. This is based on the assumption that the condensing vapors will

coat the surface of the solid seed aerosol leading to a more spherical particle (Turco, Hamill et al. 1979). As shown in Figure 32, measured depolarization ratios decrease when mixed with the various aging mechanisms for $(NH_4)_2SO_4$ and Arizona road dust.
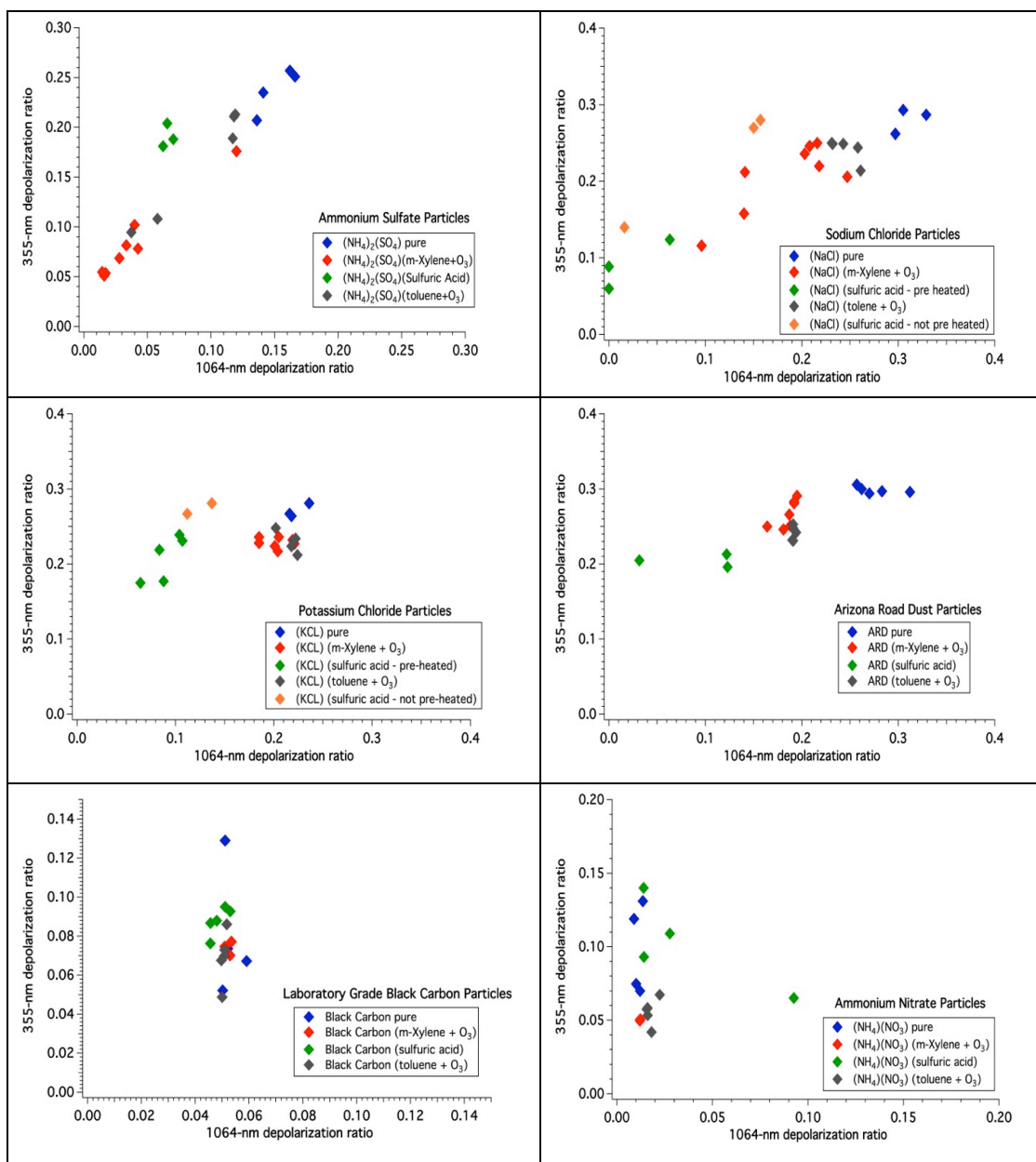
Figure 32. Measured individual depolarization ratios for all particle types studied separated by disseminated particle type. Axes are not identical for all plots.

KCl shows only a trend to a more spherical particle shape when aged by H_2SO_4. In contradiction to the assumption that aging particles become more spherical, both toluene and m-xylene byproduct aging of KCl aerosol lead to similar depolarization ratios when compared with the pure aerosol type. This result does not agree with the large decreases in scattering cross section measured for aged KCl aerosol. Similar behavior is also

46

measured for the organic aging of NaCl, although to a lesser extent. We speculate that the organic vapors are preferentially reacting chemically with the chloride aerosol rather than being adsorbed to the particle surface.   These results are further supported by the scatter plots presented in Figure 30.

A Compilation of the measured depolarization ratio results from each of the three aging mechanisms studied are given in Figure 33 alongside their purely disseminated counterparts. All plots are scaled identically for comparative purposes. Aging by H_2SO_4 deposition produces similar results for all irregular particle shapes; a decrease in depolarization ratio is observed. These results are consistent with the measured decrease in scattering cross section for particles aged by H_2SO_4 uptake.   Similar results are observed when comparing pure $(NH_4)_2SO_4$ particles with their aged counterparts.   All aging mechanisms involving $(NH_4)_2SO_4$ particles and ARD lead to a decrease in both 355-nm and 1064-nm depolarization ratios, though not as prevalent with Arizona road dust.

It is important to note that a decrease in scattering cross section can result from a decrease in the real part of the index of refraction and/or an increase in the imaginary part of the index of refraction. Many of the assumptions made in this report are based on the likelihood of an increase in particle absorption (imaginary part of the index of refraction) based on previous studies which showed that the organic uptake of atmospheric particles leads to higher absorption coefficients. However, these studies did not investigate either the chloride-based aerosol or dusts. Therefore, further experimentation is necessary to determine whether theses atmospheric particles are interacting chemically with the aging compounds or if reactive uptake is decreasing the real part of the particle index of refraction.
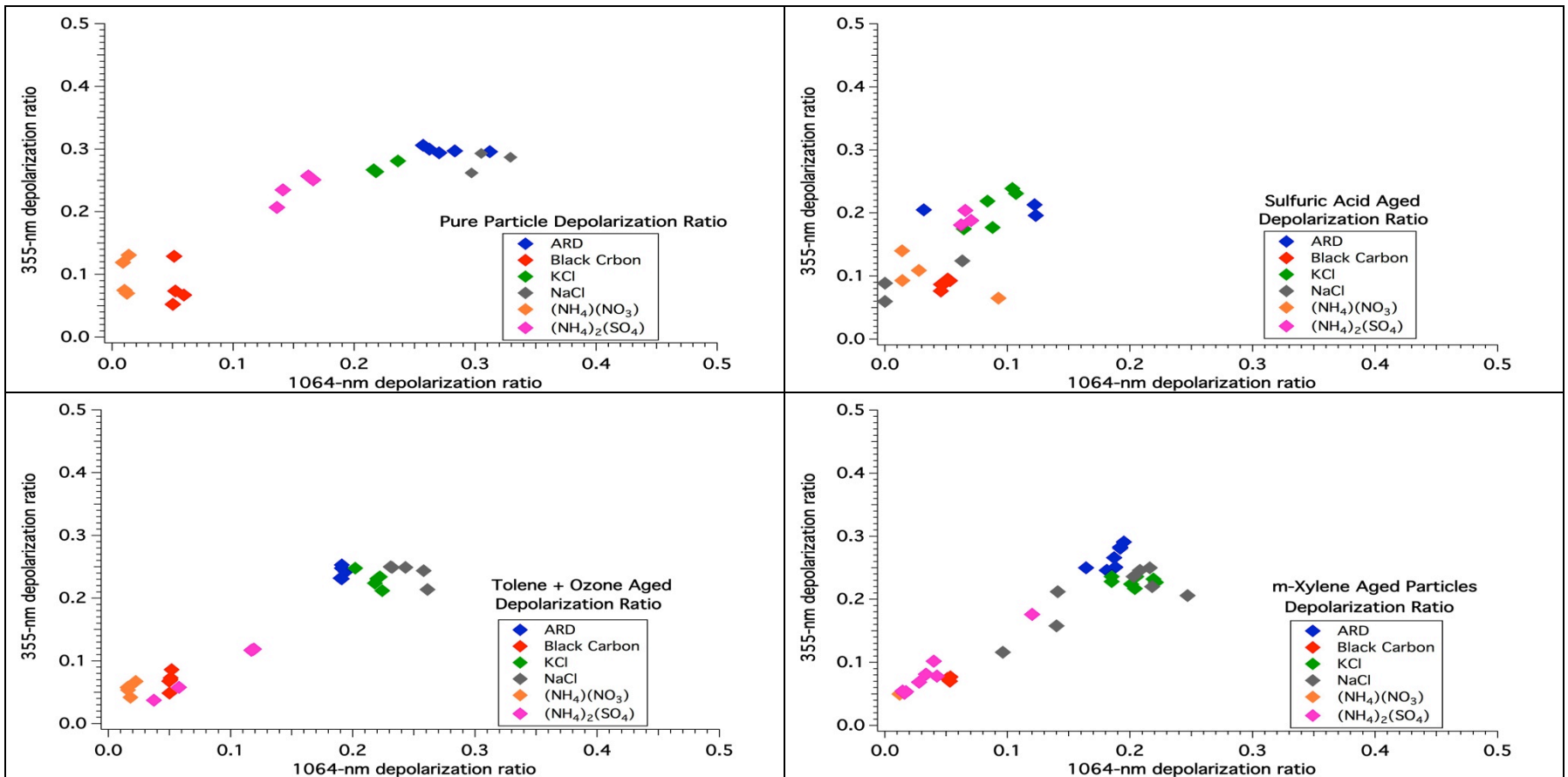
Figure 33. Comparison of measured depolarization ratio for pure particles and all aging mechanisms. Plots are separated by aging mechanism. Axes are to scale

4. SUMMARY AND CONCLUSIONS

We measured the 355-nm and 1064-nm elastic backscatter cross sections and depolarization ratios of seven different atmospherically relevant aerosols using a specially designed aerosol chamber and a bi-static LIDAR system. The seven species studied were ammonium sulfate, ammonium nitrate, sodium chloride, potassium chloride, black carbon, and Arizona road dust. Each material was disseminated into a specially designed chemical flow reactor where they were externally mixed with sulfuric acid, toluene/ozone, and m-xylene/ozone mixtures and allowed to age prior to injection into an optically accessible aerosol chamber for optical scattering measurements.   The measured optical backscatter cross sections and depolarization ratios of the aged material were then compared to their pure, un-aged counterparts in order to aid in the understanding of aerosol optical property transformation in industrial plume transport as well as general regional aerosol optical scattering influences.

Particle groupings according to general chemical composition and structure are evident for purely generated aerosol. These scattering groups were identified as salts, dust, and organic black carbon aerosol. Ammonium nitrate aerosol was unable to be grouped due to gross changes in initial size distribution and lack of repeatable measurements, although they did exhibit large backscatter cross sections compared to the other materials.   Black carbon showed the lowest measured cross sections, some 10 times lower than any other material measured, presumably due its large absorption coefficient. Depolarization ratios also revealed shape-specific groupings with dusts and crystalline salt solids having the largest measured depolarization ratios. Laboratory-grade black carbon and ammonium nitrate had the lowest depolarization ratios among the pure particle types studied, indicating that they tended to be more spherically symmetrical in shape.

In general, with the exception of potassium chloride, and to some extent sodium chloride, toluene- and m-xylene-aged aerosol exhibit a decrease in both scattering cross section and depolarization ratio. This is an indication that as these particles are aged by reactive organic uptake, they become more spherical in shape. This generalized result is not consistent with the results from potassium chloride and sodium chloride organic aging, where despite an observed decrease in scattering cross section, little if any decrease in depolarization ratio was measured. For these chloride-based particle types, aging by toluene and m-xylene ozonolysis is likely leading to a change in the bulk chemical composition of the aerosol rather than surface uptake. However, further investigation into the interactions of both potassium chloride and sodium chloride with atmospheric organic vapors is warranted to make more definitive conclusions.

Despite the differences observed in reactive uptake methods, all scattering measurements for aerosol with strong scattering signatures show that aged atmospheric aerosol can have backscatter cross section similar in magnitude to pure black carbon. This leads to an indirect conclusion, supported by literature studies of aromatic hydrocarbon absorptive properties, that these aerosols can be as efficient at light absorption in the 355-nm and 1064-nm wavelengths as pure black carbon aerosol.   This result has large implications for climate related research and global climate modeling efforts as these aerosol will likely impact atmospheric global warming

coefficients. Dusts in particular have an aged scattering cross section nearly equal to that of pure black carbon. Since dusts are often transported globally from developing industrial areas such as Asia, dust settling in the Arctic must be included in sea-ice and artic warming models. In addition, with toluene being one of the most abundant anthropogenically produced organic gas, increased efforts to correctly model the scattering and absorption of plume aerosol and transport is necessary to help understand the impact of secondary aerosol on regional and global climate. Furthermore, additional studies investigating the timescales of organic aerosol production within industrial plume transport can aid in measuring plume age from space borne LIDAR observations.

5. REFERENCES

Andreae, M., et al. (2001). "Transport of biomass burning smoke to the upper troposphere by deep convection in the equatorial region." Geophysical Research Letters **28**(6): 951-954.

Andreae, M. O. and A. Gelencsér (2006). "Black carbon or brown carbon? The nature of light-absorbing carbonaceous aerosols." Atmos. Chem. Phys. **6**(10): 3131-3148.

Bahreini, R., et al. (2005). "Measurements of Secondary Organic Aerosol from Oxidation of Cycloalkenes, Terpenes, and m-Xylene Using an Aerodyne Aerosol Mass Spectrometer." Environmental Science & Technology **39**(15): 5674-5688.

Baltaretu, C. O., et al. (2008). "Primary Atmospheric Oxidation Mechanism for Toluene." The Journal of Physical Chemistry A **113**(1): 221-230.

Bloss, C., et al. (2005). "Development of a detailed chemical mechanism (MCMv3.1) for the atmospheric oxidation of aromatic hydrocarbons." Atmos. Chem. Phys. **5**(3): 641-664.

Buzcu, B. and M. P. Fraser (2006). "Source identification and apportionment of volatile organic compounds in Houston, TX." Atmospheric Environment **40**(13): 2385-2400.

Colarco, P. R., et al. (2004). "Transport of smoke from Canadian forest fires to the surface near Washington, D.C.: Injection height, entrainment, and optical properties." Journal of Geophysical Research: Atmospheres **109**(D6): D06203.

Czoschke, N. M., et al. (2003). "Effect of acidic seed on biogenic secondary organic aerosol growth." Atmospheric Environment **37**(30): 4287-4299.

Donahue, N. M., et al. (2009). "Atmospheric organic particulate matter: From smoke to secondary organic aerosol." Atmospheric Environment **43**(1): 94-106.

Duce, R., et al. (1980). "Long-range atmospheric transport of soil dust from Asia to the tropical North Pacific- Temporal variability." Science **209**(4464): 1522-1524.

Finlayson-Pitts, B. J. and J. N. Pitts (1997). "Tropospheric Air Pollution: Ozone, Airborne Toxics, Polycyclic Aromatic Hydrocarbons, and Particles." Science **276**(5315): 1045-1051.

Hallquist, M., et al. (2009). "The formation, properties and impact of secondary organic aerosol: current and emerging issues." Atmos. Chem. Phys. **9**(14): 5155-5236.

Hitchcock, D. R., et al. (1980). "Sulfuric acid aerosols and HCl release in coastal atmospheres: Evidence of rapid formation of sulfuric acid particulates." Atmospheric Environment (1967) **14**(2): 165-182.

Hurley, M. D., et al. (2001). "Organic Aerosol Formation during the Atmospheric Degradation of Toluene." Environmental Science & Technology **35**(7): 1358-1366.

Inaba, H. and T. Kobayasi (1972). "Laser-Raman radar—Laser-Raman scattering methods for remote detection and analysis of atmospheric pollution." Opto-electronics **4**(2): 101-123.

Jang, M., et al. (2003). "Organic aerosol growth by acid-catalyzed heterogeneous reactions of octanal in a flow reactor." Atmospheric Environment **37**(15): 2125-2138.

Kleinman, L. I., et al. (2002). "Ozone production rate and hydrocarbon reactivity in 5 urban areas: A cause of high ozone concentration in Houston." Geophysical Research Letters **29**(10): 105-101-105-104.

Kovalev, V. A. and W. E. Eichinger "Atmospheric Parameters from Elastic Lidar Data." Elastic Lidar: Theory, Practice, and Analysis Methods: 431-505.

Kroll, J. H., et al. (2005). "Chamber studies of secondary organic aerosol growth by reactive uptake of simple carbonyl compounds." Journal of Geophysical Research: Atmospheres **110**(D23): D23207.

Matsson, J. E. and J. Matsson (2012). An Introduction to SolidWorks® Flow Simulation 2012, SDC Publications.

Menon, S., et al. (2002). "Climate Effects of Black Carbon Aerosols in China and India." Science **297**(5590): 2250-2253.

Odum, J. R., et al. (1996). "Gas/Particle Partitioning and Secondary Organic Aerosol Yields." Environmental Science & Technology **30**(8): 2580-2585.

Pfeiffer, T., et al. (1998). "Tropospheric OH formation by ozonolysis of terpenes." Chemical Physics Letters **298**(4–6): 351-358.

Rodhe, H., et al. (1981). "Formation of sulfuric and nitric acid in the atmosphere during long-range transport." Tellus **33**(2): 132-141.

Ryerson, T. B., et al. (2003). "Effect of petrochemical industrial emissions of reactive alkenes and NOx on tropospheric ozone formation in Houston, Texas." Journal of Geophysical Research: Atmospheres **108**(D8): 4249.

Shapiro, E. L., et al. (2009). "Light-absorbing secondary organic material formed by glyoxal in aqueous aerosol mimics." Atmos. Chem. Phys. **9**(7): 2289-2300.

Suh, I., et al. (2003). "Oxidation Mechanism of Aromatic Peroxy and Bicyclic Radicals from OH−Toluene Reactions." Journal of the American Chemical Society **125**(41): 12655-12665.

Turco, R. P., et al. (1979). "A One-Dimensional Model Describing Aerosol Formation and Evolution in the Stratosphere: I. Physical Processes and Mathematical Analogs." Journal of the Atmospheric Sciences **36**(4): 699-717.

Uematsu, M., et al. (1983). "Transport of mineral aerosol from Asia over the North Pacific Ocean." Journal of Geophysical Research **88**(C9): 5343-5352.

Wang, S.-C., et al. (1992). "Aerosol formation and growth in atmospheric organic/NOχ systems—I. Outdoor smog chamber studies of C7- and C8-hydrocarbons." Atmospheric Environment. Part A. General Topics **26**(3): 403-420.

Zhang, X., et al. (2011). "Light-absorbing soluble organic aerosol in Los Angeles and Atlanta: A contrast in secondary organic aerosol." Geophysical Research Letters **38**(21): L21810.

Zhao, W., et al. (2004). "Source Identification of Volatile Organic Compounds in Houston, Texas." Environmental Science & Technology **38**(5): 1338-1347.

DISTRIBUTION

1	MS0124	John Mitchner	8004
1	MS0701	Marianne Walck	6900
1	MS0735	John Merson	6910
1	MS0762	Bradley Parks	6630
1	MS0782	Paul Smith	6633
1	MS1148	Andres Sanchez	6633
1	MS1423	William Seng	1118
1	MS1423	Randy Schmitt	1118
1	MS0359	D. Chavez, LDRD Office	1911
1	MS0899	Technical Library	9536 (electronic copy)

Sandia National Laboratories